

Multilepton Signatures from Dark Matter at the LHC

Alexander Belyaev,^{1,2,*} Ulla Blumenschein,^{3,†} Arran Freegard,^{1,3,‡} Stefano Moretti,^{1,2,4,§} and Dipan Sengupta^{5,6,¶}

¹*School of Physics and Astronomy, University of Southampton, Highfield. Southampton SO17 1BJ, United Kingdom*

²*Particle Physics Department, Rutherford Appleton Laboratory, Chilton, Didcot, Oxon OX11 0QX, United Kingdom*

³*Particle Physics Research Centre, School of Physical and Chemical Sciences, Queen Mary University of London, Mile End Road, London E1 4NS, United Kingdom*

⁴*Department of Physics and Astronomy, Uppsala University, Box 516, SE-751 20 Uppsala, Sweden*

⁵*Department of Physics and Astronomy, University of California, San Diego 9500 Gilman Drive, La Jolla, California-92037, United States of America*

⁶*ARC Centre of Excellence for Dark Matter Particle Physics, Department of Physics, University of Adelaide, South Australia 5005, Australia*

(Dated: April 14, 2022)

Abstract

Leptonic signatures of Dark Matter (DM) are one of the cleanest ways to discover such a secluded form of matter at high energy colliders. We explore the full parameter space relevant to multi-lepton (2- and 3-lepton) signatures at the Large Hadron Collider (LHC) from representative minimal consistent models with scalar and fermion DM. In our analysis, we suggest a new parametrisation of the model parameter spaces in terms of the DM mass and mass differences between DM and its multiplet partners. This parametrisation allows us to explore properties of DM models in their whole parameter space. This approach is generic and quite model-independent since the mass differences are related to the couplings of the DM to the Standard Model (SM) sector. We establish the most up-to-date LHC limits on the inert 2-Higgs Doublet Model (i2HDM) and Minimal Fermion DM (MFDM) model parameter spaces, by using the complementary information stemming from 2- and 3-lepton signatures. We provide a map of LHC efficiencies and cross-section limits for such 2- and 3-lepton signatures allowing one to easily make model-independent reinterpretations of LHC results for analogous classes of models. We also present combined constraints from the LHC, DM relic density and direct search experiments indicating the current status of the i2HDM and MFDM model.

* a.belyaev@phys.soton.ac.uk

† u.blumenschein@qmul.ac.uk

‡ acf1g14@soton.ac.uk

§ s.moretti@soton.ac.uk

¶ disengupta@physics.ucsd.edu

CONTENTS

I. Introduction	3
II. Models	4
A. MFDM Model	4
B. i2HDM	6
III. Signal Processes	7
IV. Results	13
A. LHC Searches and Tools	13
B. Constraints on the i2HDM and MFDM Model	14
1. Constraints on the i2HDM channels	15
2. Constraints on the MFDM Model Channels	17
C. Complementarity between the LHC and Non-collider Experiments	20
V. Conclusions	23
Acknowledgements	24
A. 8 TeV Validation: i2HDM	25
B. i2HDM 13 TeV, 2- or 3-lepton Final states	28
C. MFDM 8 TeV	30
D. Numerical Overlaid Plots	32
E. Sample Exclusion Formulae	34
F. i2HDM Cross-Section Limits	35
G. MFDM Cross-Section Limits	38
H. Example Analyses and Cutflows	47
References	48

I. INTRODUCTION

The nature of Dark Matter (DM) is one of the greatest puzzles of modern particle physics and cosmology. While overwhelming observational evidences from galactic to cosmological scales point to the existence of DM [1–3], after decades of experimental effort, only its gravitational interaction has been confirmed. At the moment, we do not have information about DM properties, such as its mass, spin, interactions (other than gravitational), symmetry responsible for its stability, number of states associated to it and possible particles that would mediate the interactions between DM and the Standard Model (SM) particles.

If DM is light enough and interacts with SM particles directly, or via some mediators with a strength beyond the gravitational one, its elusive nature can be detected or constrained in direct production at colliders, complementing direct and indirect DM searches in non-collider experiments. Therefore, the search for DM is one of the top priorities of the Large Hadron Collider (LHC) [4] programme and that of future collider experiments.

The most general DM signature at colliders is the mono- X one, where X stands for a SM object, such as jet, Higgs, Z , W , photon, top-quark, etc. that recoils against the missing energy from the DM pair. This signature has limitations, though, especially if there are no light mediators decaying into a DM pair which could enhance the corresponding signal to compete with the large SM background from $Z \rightarrow \nu\nu$. If such mediators are absent or very heavy even the High-Luminosity LHC (HL-LHC) [5] could probe the DM mass only up to about 250 GeV, as shown, e.g., for the case of higgsino DM in the Minimal Supersymmetric Standard Model (MSSM) [6–9]. This limitation motivates us to look for signatures beyond the mono- X one.

This study is devoted to a generic class of DM models, where the DM is a part of an Electro-Weak (EW) multiplet and the mass splitting between DM (D_1) and its charged partner(s) (D^+ , ...) or next-to-lightest neutral partners (D_2 , ...) is large enough so as to give rise to multi-lepton signatures at the LHC from processes such as $pp \rightarrow D_1 D^\pm$, $pp \rightarrow D^+ D^-$, $pp \rightarrow D_1 D_2$, $pp \rightarrow D^\pm D_2$ and $pp \rightarrow D_2 D_2$, which are then followed by the D^\pm and D_2 decays to gauge or Higgs bosons which in turn decay into leptons.

These signatures with visible 1-4 lepton(s) and Missing Transverse Energy (MET) can be observed for $\Delta m^+ = m_{D^\pm} - m_{D_1}$ and/or $\Delta m^0 = m_{D_2} - m_{D^\pm}$ above a few GeV. The case when Δm^+ is of the order of the pion mass – when D^+ and D_1 are degenerate at tree-level and their mass split is generated radiatively, due to the quantum corrections involving a loop of the photon and the charged DM multiplet partner(s) – leads to a compelling complementary signature with disappearing tracks which was recently studied in detail in [10].

The 2- and 3-lepton signatures from DM models have been previously explored in the context of the inert 2-Higgs-Doublet Model (i2HDM) [11], Supersymmetric scenarios [12, 13] (including those with sneutrino DM [14]) or models with vector-like leptonic DM [15]. These earlier studies have mainly explored the one or two-dimensional parameter space of specific DM models, or just selected benchmark points from their multi-dimensional parameter space. Our study presents the following new results on multi-lepton signatures from DM at the LHC:

- we explore the full three-dimensional parameter space relevant to the LHC for two representative minimal consistent DM models with DM of spin-0 and -1/2, respectively: the i2HDM and Minimal Fermion DM (MFDM) model, respectively, and present the sensitivity of recent LHC data to these;
- we suggest a new parametrisation for both models which allows one to better understand and interpret their properties and visualise the no-loose theorem in their full parameter space;

- we find that the 3-lepton signature becomes relevant for large $D^+ - D$ mass gaps and adds important and complementary sensitivity to the LHC searches;
- we implement and validate the 8 TeV ATLAS [16] multi-lepton analysis of Ref. [17] in CheckMATE [18] relevant to our study and made available those analyses to the community;
- we create a map of the LHC efficiencies and the cross-section limits for 2- and 3-lepton signatures in the simple parameter space expressed through the DM mass and the $D^+ - D$ and $D_2 - D^+$ mass differences which can be used for generic reinterpretation of spin-0 and spin-1/2 DM models.

The rest of the paper is organized as follows: in section II we present the DM models under study, in section III we discuss details of the signal processes leading to 2- and 3-lepton signatures, in section IV we present details of the analysis, including the implementation into the CheckMATE package, and the new LHC sensitivity to the parameter space of the two models under study while in section V we draw our conclusions. Furthermore, details of our study are given in Appendices A–E, including the respective plots on the exclusion of the parameter space (Appendix D) and tables with the efficiencies and cross-section limits expressed in terms of universal parameters such as the DM mass and the $D^+ - D$ and $D_2 - D^+$ mass differences which can be applied for generic reinterpretation of spin-0 and spin-1/2 DM models (Appendices F–G).

II. MODELS

In the following subsections, II A and II B, we present the models under study in this work. Both of these are phenomenologically well-motivated and can be mapped onto well-known Supersymmetric scenarios. They are minimal in nature, due to the small number of parameters that impact the phenomenology, in terms of both collider and DM considerations.

For the purposes of this paper, where we are interested primarily in the collider phenomenology of the model, we do not initially impose strict requirements on relic density and (in)direct detection of DM. Rather, we first set out the collider constraints independently of DM considerations. Only eventually we show how the latter impact the parameter space, in order to illustrate that these are complementary to collider constraints.

A. MFDM Model

The Lagrangian for the MFDM model, which augments the SM by an EW fermion (ψ) doublet of χ_1^0 , χ_2^0 and χ^+ as well as a Majorana singlet fermion χ_s^0 , is [19]

$$\mathcal{L}_{\text{MFDM}} = \mathcal{L}_{\text{SM}} + \bar{\psi}(i\not{D} - m_\psi)\psi + \frac{1}{2}\bar{\chi}_s^0(i\not{\partial} - m_s)\chi_s^0 - (Y_{\text{DM}}(\bar{\psi}\Phi\chi_s^0) + h.c.). \quad (1)$$

The fermion $SU(2)$ doublet is

$$\psi = \begin{pmatrix} \chi^+ \\ \frac{1}{\sqrt{2}}(\chi_1^0 + i\chi_2^0) \end{pmatrix} \quad (2)$$

while the Higgs doublet Φ , after EW Symmetry Breaking (EWSB), is

$$\Phi = \begin{pmatrix} 0 \\ \frac{1}{\sqrt{2}}(v + h) \end{pmatrix}, \quad (3)$$

where h is the SM-like Higgs boson with a mass of 125 GeV, while $v = 246$ GeV is Vacuum Expectation Value (VEV) of the SM Higgs potential. We impose a \mathcal{Z}_2 odd parity on the EW fermion doublet as well as the Majorana singlet fermion, such that the lightest particle after diagonalisation of the fermion mass matrix is stable and a DM candidate. Note that, in the model as written above, we assume that χ_1^0, χ_2^0 are Majorana fermions. The DM relic density requirements are satisfied by the usual freeze-out mechanism by scatterings mediated by the Z or Higgs boson. The minimality of this model is manifest in the fact there are only 3 new parameters, m_ψ, Y_{DM} and m_s .

Note that χ_1^0 and χ_s^0 mix via Yukawa couplings while χ_2^0 and χ^+ are mass degenerate. The physical masses are then obtained by diagonalisation of the mass matrix from the $(\chi_s^0, \chi_1^0, \chi_2^0)$ interaction basis to the (D, D_2, D') mass basis as

$$M = \begin{pmatrix} m_\psi & Y_{\text{DM}}v & 0 \\ Y_{\text{DM}}v & m_s & 0 \\ 0 & 0 & m_\psi \end{pmatrix}. \quad (4)$$

The mass matrix is thus diagonalised by one rotation angle θ of the upper 2×2 block, while we identify $m_\psi = m_{D+}$.

The rotation angle θ that diagonalises the mass matrix can be expressed in terms of two useful relations,

$$\tan 2\theta = \frac{2Y_{\text{DM}}v}{m_\psi - m_s}, \quad (5)$$

$$\sin 2\theta = -\frac{2Y_{\text{DM}}v}{m_{D_2} - m_D} \quad (6)$$

and the connection between gauge eigenstates χ_s^0 and χ_1^0 and mass eigenstates D and D_2 is given by

$$\begin{aligned} \chi_s^0 &= D \sin \theta + D_2 \cos \theta, \\ \chi_1^0 &= D \cos \theta - D_2 \sin \theta. \end{aligned} \quad (7)$$

The connection between physical masses and mass parameters in the Lagrangian is given by

$$\begin{aligned} m_s &= m_D + m_{D_2} - m_{D+}, \\ m_\psi &= m_{D+} = m_{D'}. \end{aligned} \quad (8)$$

The mass splitting between m_{D_1} and m_{D_3} is related to the Yukawa coupling Y_{DM} via

$$Y_{\text{DM}} = \frac{\sqrt{(m_{D_2} - m_{D+})(m_{D+} - m_D)}}{v} = \frac{\sqrt{\Delta m^0 \Delta m^+}}{v}, \quad (9)$$

where

$$\Delta m^0 = m_{D_2} - m_{D+}, \quad \Delta m^+ = m_{D+} - m_D. \quad (10)$$

The requirement that Y_{DM} must be real leads to the following mass ordering:

$$m_{D_2} \geq m_{D+} = m_{D'} > m_D. \quad (11)$$

The parameter space of the model can be expressed in terms of three physical masses:

$$\{m_D, m_{D'} = m_{D\pm}, m_{D_2}\}. \quad (12)$$

However, since the Yukawa coupling controls the mass splitting as well as DM mixing and therefore the strength of the interactions between DM and SM, it is also convenient to trade parameters and parametrise the model space using the following set

$$\{m_D, \Delta m^+, \Delta m^0\}_{\text{MFDM}}, \quad (13)$$

which consists of the DM mass and two mass splittings between D^+ and DM as well as between D_2 and D^+ . As we will see, the latter parametrisation allows to better visualise and interpret collider search results for the whole parameter space. The model is also subject to various theoretical constraints, like perturbativity and radiative stability, which are satisfied for the couplings and masses adopted in this paper.

As far as DM constraints are concerned, we first assess direct detection constraints. Since there is no tree level Z boson interaction with the DM candidate, the spin-independent direct detection constraint only arises from DM-nucleon scattering controlled by the Higgs coupling to DM. By controlling the mass splitting, this coupling can be made small, leaving a viable parameter space. In order to obtain the correct (not over-abundant) relic abundance, one needs an efficient annihilation mechanism via the Higgs funnel $m_D \simeq m_{h/2}$. These considerations were previously taken into account in a previous paper [19].

B. i2HDM

This scenario [20–22] introduces a second scalar doublet ϕ_2 to the SM Higgs sector, with the same quantum numbers as the SM Higgs doublet ϕ_1 . However, a discrete Z_2 odd symmetry is imposed on the second doublet such that there are no direct coupling to fermions, rendering it ‘inert’.

In the unitary gauge, the two scalar doublets can be written as

$$\phi_1 = \frac{1}{\sqrt{2}} \begin{pmatrix} 0 \\ v + H \end{pmatrix}, \phi_2 = \frac{1}{\sqrt{2}} \begin{pmatrix} \sqrt{2}D^+ \\ D_1 + iD_2 \end{pmatrix}, \quad (14)$$

where D_1 , D_2 and D^+ are the lightest, next-to-lightest and charged inert scalars, respectively. Within this parametrisation, the Z_2 symmetry is preserved due to the fact that $v_2 = 0$ and the absence of Yukawa couplings of the ϕ_2 to fermions. This ‘inert minimum’, for $\langle \phi_i^0 \rangle = \frac{v_i}{\sqrt{2}}$, corresponds to $v_1 = v$ and $v_2 = 0$. This symmetry provides the stability of the lightest inert boson against decaying into SM particles, which makes D_1 a DM candidate.

The scalar Lagrangian is then given by

$$\mathcal{L}_\phi = |D_\mu \phi_1|^2 + |D_\mu \phi_2|^2 - V(\phi_1, \phi_2), \quad (15)$$

where the most general scalar potential is written as

$$\begin{aligned} V(\phi_1, \phi_2) = & -m_1^2(\phi_1^\dagger \phi_1) - m_2^2(\phi_2^\dagger \phi_2) + \lambda_1(\phi_1^\dagger \phi_1)^2 + \lambda_2(\phi_2^\dagger \phi_2)^2 + \lambda_3(\phi_1^\dagger \phi_1)(\phi_2^\dagger \phi_2) \\ & + \lambda_4(\phi_2^\dagger \phi_1)(\phi_1^\dagger \phi_2) + \frac{\lambda_5}{2}[(\phi_1^\dagger \phi_2)^2 + (\phi_2^\dagger \phi_1)^2] \end{aligned} \quad (16)$$

and contains all of the scalar interactions allowed by the Z_2 symmetry. Here, all mass and coupling parameters are defined to be positive. Under the

$$m_{D_1}^2 > (\lambda_{345}/2 - \sqrt{\lambda_1 \lambda_2})v^2 \quad (17)$$

condition [23], where m_{D_1} is the mass of D_1 and $\lambda_{345} = \lambda_3 + \lambda_4 + \lambda_5$,

The physical masses are given by (λ_5 can always be chosen positive due to the $\phi_2 \rightarrow i\phi_2$, $\lambda_5 \rightarrow -\lambda_5$ symmetry)

$$m_{D_1}^2 = \frac{1}{2}(\lambda_3 + \lambda_4 - \lambda_5)v^2 - m_2^2, \quad m_{D_2}^2 = \frac{1}{2}(\lambda_3 + \lambda_4 + \lambda_5)v^2 - m_2^2, \quad m_{D^\pm}^2 = \frac{1}{2}\lambda_3v^2 - m_2^2, \quad (18)$$

which, together with λ_{345} and λ_2 , parametrise completely the DM sector of the model, described by five parameters:

$$m_{D_1}, m_{D_2}, m_{D^\pm}, \lambda_{345}, \lambda_2. \quad (19)$$

These can be further reduced for this analysis, by noting that λ_2 does not affect the LHC phenomenology under study at all since it controls DM the self-interaction only.

Furthermore, we also exclude λ_{345} from our analysis for the following reason. The relevant coupling for the $gg \rightarrow H^* \rightarrow D^+D^-$ and $gg \rightarrow H^* \rightarrow D_2D_2$ processes are λ_3 and $\lambda_3 + \lambda_4 - \lambda_5$, respectively, which are limited by EW precision tests plus perturbativity [23, 24] and related to the mass splitting between D^+ and D_2 . We have checked that, even if we maximise the cross section of either of the two processes by increasing the respective coupling up to the maximal allowed value, the respective cross section¹ will still be below the signal production cross section via the weak coupling. Moreover, the value of the λ_{345} coupling is also strongly limited by DM direct detection constraints as well as by limits on the invisible Higgs boson decay branching ratio in the case when $m_H > 2m_{D_1}$ (see, e.g., [23, 25]). Therefore, in order to establish a conservative and generic limit on the i2HDM parameter space, we exclude λ_{345} from the current study and set its value to zero. Therefore, the parameter space we focus on is three-parametric:

$$m_{D_1}, m_{D_2}, m_{D^\pm}, \quad (20)$$

which can easily be visualised in 2D planes, while fixing one parameter. In analogy with the MFDM model we also use the

$$\{m_{D_1}, \Delta m^+, \Delta m^0\}_{\text{i2HDM}} \quad (21)$$

parametrisation, where

$$\Delta m^0 = m_{D_2} - m_{D^\pm}, \quad \Delta m^+ = m_{D^\pm} - m_{D_1}, \quad (22)$$

which allows an even better visualisation and interpretation of the model parameter space. We note one important caveat here. Note that we deliberately choose the mass hierarchy $m_{D_2} > m_{D^\pm} > m_{D_1}$, such that D_1 is the lightest state. This choice is motivated by phenomenological reasons in order to bring out the intricacies of the collider constraints set by 2- and 3-lepton searches. The other hierarchy $m_{D^\pm} > m_{D_2} > m_{D_1}$ is entirely feasible and will lead to constraints comparable to the ones described in this paper. We leave this possibility for a future work.

III. SIGNAL PROCESSES

In this section, we study production and decay processes inclusively, the combination of which gives an idea about the LHC event rate of the signatures under study. Specifically, we study lepton signatures from DM multiplet partners generically appearing when the mass splitting between DM and those partners is large enough to give rise to sufficiently energetic leptons, which can originate from the following processes:

¹ Both cross sections cannot be simultaneously made large since either D^+ or D_2 should be heavier than the other, which would make one of the cross sections much smaller than the other.

- $pp \rightarrow D_1 D^\pm \rightarrow D_1 D_1 W^{\pm(*)} \rightarrow D_1 D_1 \ell^\pm \nu$
- $pp \rightarrow D^+ D^- \rightarrow D_1 D_1 W^{+(*)} W^{-(*)} \rightarrow D_1 D_1 \ell^+ \ell^- \nu \bar{\nu}$
- $pp \rightarrow D_1 D_n \rightarrow D_1 D_1 Z^{(*)} \rightarrow D_1 D_1 \ell^+ \ell^-$
- $pp \rightarrow D^\pm D_n \rightarrow D_1 D_1 Z^{(*)} W^{\pm(*)} \rightarrow D_1 D_1 \ell^+ \ell^- \ell^\pm \nu$
- $pp \rightarrow D^\pm D_n \rightarrow D_1 D_1 W^\pm H \rightarrow D_1 D_1 W^\pm W^\pm W^\mp \rightarrow D_1 D_1 \ell^\pm \ell^\pm \ell^\mp \nu \nu \nu$
- $pp \rightarrow D_n D_n \rightarrow D_1 D_1 Z^{(*)} Z^{(*)} \rightarrow D_1 D_1 \ell^+ \ell^- \ell^+ \ell^- / D_1 D_1 \ell^+ \ell^- q \bar{q}$

where $D_n = D_2$ or $D_n = D', D_2$ depending on the scenario, i2HDM or MFDM model, respectively. Since D^\pm and D_n decay via Z or W^\pm either hadronically or leptonically in association with the DM candidate, they can provide signatures with several charged leptons plus MET, which are the subject of this study.

The common diagrams for both models under study for the signal production processes

$$q\bar{q} \rightarrow D^+ D^- \quad \text{and} \quad q\bar{q}' \rightarrow D^\pm D_2 \quad (23)$$

that provide the multi-lepton signatures we study here are presented in Fig. 1. In addition to these

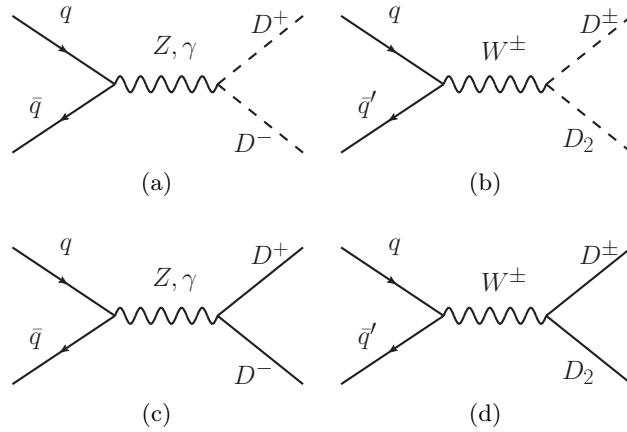


FIG. 1: Feynman diagrams for $D^+ D^-$ and $D^\pm D_2$ production common to the i2HDM (top) and MFDM model (bottom).

common Feynman diagrams, the $ZD_2 D_1$ and $ZZD_1 D_1$ vertices, specific only to the i2HDM, provides additional Feynman diagrams and corresponding new kinematic topologies, shown in Fig. 2(a) and (b). Conversely, since the MFDM model has an additional neutral DM partner, D' , in contrast to the i2HDM, there are additional MFDM processes²,

$$q\bar{q} \rightarrow D' D_1, \quad q\bar{q} \rightarrow D_2 D' \quad \text{and} \quad q\bar{q}' \rightarrow D^\pm D', \quad (24)$$

providing the required multi-lepton signatures through the topologies shown in Fig. 2(c), (d) and (e), respectively.

The cross sections for the above production processes presented here are calculated using CalcHEP [26], a package designed for the evaluation of the tree-level processes and their respective

² MFDM also allows for $D_2 D_1$ production through the $HD_2 D_1$ vertex, but we do not study this production mode as it is highly suppressed compared to the other processes discussed here.

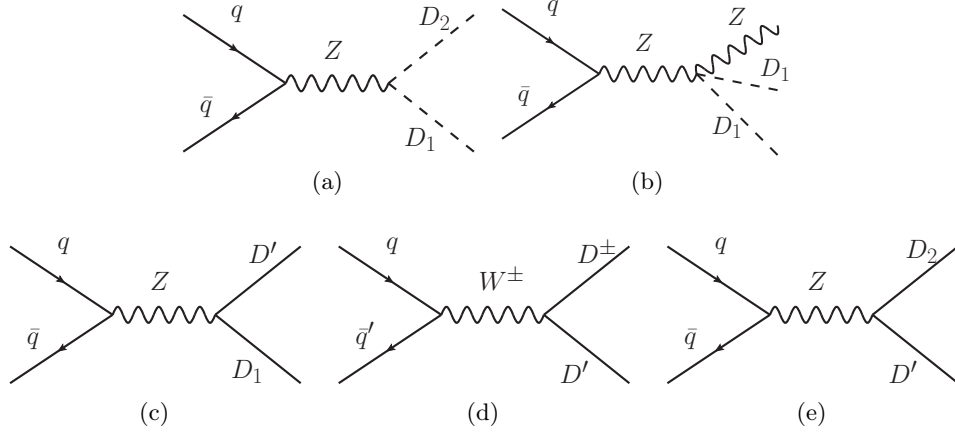


FIG. 2: Feynman diagrams for D_2D_1 , ZD_1D_1 production exclusive to the i2HDM, (a) and (b), and for D_1D' , $D^\pm D'$ and D_2D' production exclusive to the MFDM model, (c), (d) and (e).

Monte Carlo (MC) simulation. CalcHEP exploits the Beyond the SM (BSM) scenarios implemented on the HEPMDB [27], allowing to cross check these in different gauges for the purpose of validating the relevant implementation, and further has an interface to LHAPDF [28] for a wide selection of Parton Distribution Functions (PDFs), allowing to ascertain the dominant systematic error on the theoretical side³. The events generated by CalcHEP in Les Houches Event (LHE) format can then be used by other tools enabling further simulations of the parton shower and detector effects. For the latter, we use here the combination PYTHIA [29] and DELPHES [30], respectively.

The relevant cross sections are presented in Fig. 3 as a function of the Δm^+ parameter for a 100 GeV DM mass and two values of $\Delta m^0=1$ and 100 GeV (left and right panels, respectively) for the i2HDM (top panels) and MFDM model (bottom panels). Here, one can see that for $\Delta m^0=1$, D_1D_2 production has the highest rate for the i2HDM while, in the case of the MFDM model, the analogous D_1D' channel is highly suppressed. This can be explained by the fact that the ZD_1D_2 coupling controlling this process in the i2HDM model is just a pure (weak) gauge coupling while in the MFDM model the ZD_1D' coupling is the product of a (weak) gauge coupling and the cosine of the $\chi_1^0 - \chi_s^0$ mixing angle, which is suppressed when $\Delta m^+ \gg \Delta m^0 = 1$, as shown by the blue line in Fig. 4(b).

In contrast, for $\Delta m^0=1$ GeV, the production cross sections for D^+D^- , D_2D^\pm and $D'D^\pm$ (represented by red, green and brown lines, respectively) are close to each other in each model. This can be explained by the fact that the D^+ and D_2 masses are about the same as well as the couplings controlling these processes (which are purely (weak) gauge ones). Furthermore, one should note that the ZZD_1D_1 coupling (unique to the i2HDM) contributes to ZD_1D_1 production, the $2 \rightarrow 3$ process with a subdominant cross section in comparison with $2 \rightarrow 2$ production. However, when the $D_2 \rightarrow ZD_1$ decay is open, the ZD_1D_1 process will include the corresponding resonant $2 \rightarrow 2$ production and decay. Therefore, to avoid double counting, we do not present the cross section for this $2 \rightarrow 3$ process in Fig. 3(a).

For the MFDM model, the additional production process $D'D_2$ (pink line), characteristic of this scenario, has a similar cross section to D^+D^- and $D'D^\pm$ for the very same reason. One should also note that the cross sections for scalar DM production are smaller than those for fermion DM production by the spin factor $\beta^2/4$ (where $\beta = \sqrt{1 - (m_{D_i} + m_{D_j})^2/\hat{s}}$ with m_{D_i} and m_{D_j} being

³ Note that the production and decay processes exploited here are EW in nature, so that the QCD corrections to these are small, typically of order 20%, and their residual uncertainty negligible.

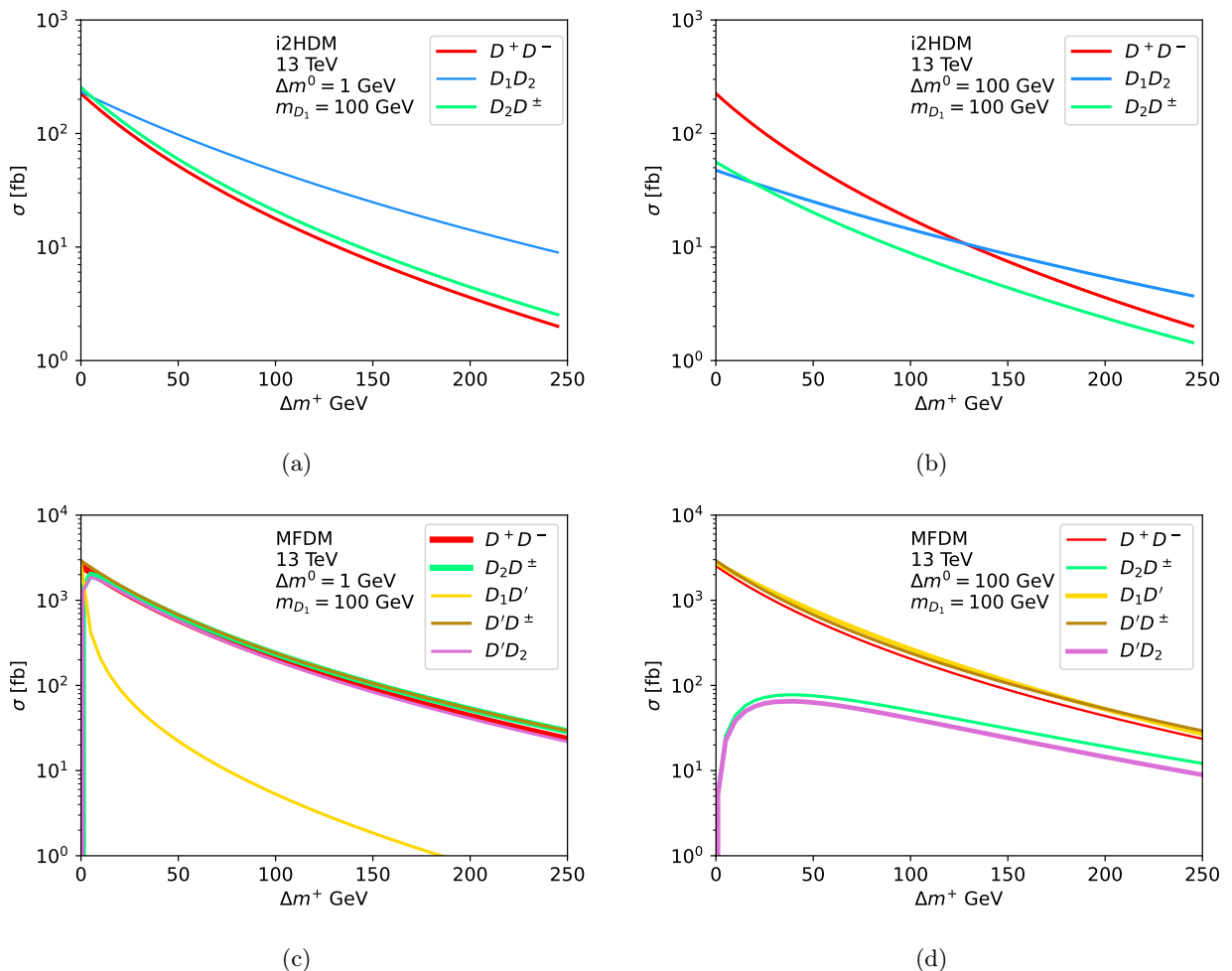


FIG. 3: The cross sections for pair production of DM partners for the i2HDM (top) and MFDM model (bottom) for $\Delta m^0 = 1$ and 100 GeV (left and right panels, respectively).

the masses of DM particles in the final state), which ranges from about 1/4 to about 1/10, as one can see from Fig. 3 (left panels).

Let us now consider the $\Delta m^0=100$ GeV case presented in the right panels of Fig. 3. In the i2HDM, the $\Delta m^0 = 1 \rightarrow 100$ GeV change (which increases the D_2 mass) equally suppresses D_1D_2 and D_2D^\pm production by about a factor of 4. For the MFDM model, the $\Delta m^0 = 1 \rightarrow 100$ GeV change affects both the D_2 mass (see Eq. (10)) and the $\chi_1^0 - \chi_s^0$ mixing angle θ (the ZD_2D' and $W^+D_2D^-$ couplings are both proportional to $\sin\theta$), leading to a suppression of $D'D_2$ and D_2D^\pm production from both causes (see pink and green lines, respectively, in Fig. 3(d)). In contrast, D_1D' production is enhanced, since it is proportional to $\cos^2\theta$, which increases with Δm^0 (see Fig. 4(b)). Finally, the D^+D^- processes are not affected by a Δm^0 variation in both models. One should also note that in the MFDM model $D'D^\pm$ is also not affected by a Δm^0 variation since such a variation does change neither the D' mass nor the $W^+D'D^-$ coupling (which is purely weak and is not affected by the $\chi_1^0 - \chi_s^0$ mixing).

In order to get an idea of the rate at which leptons are produced in the final state we also need to discuss Branching Ratios (BRs) of decay chains leading to DM particles and connect these with their pair production cross sections. In Fig. 5, we present the decay patterns common to both

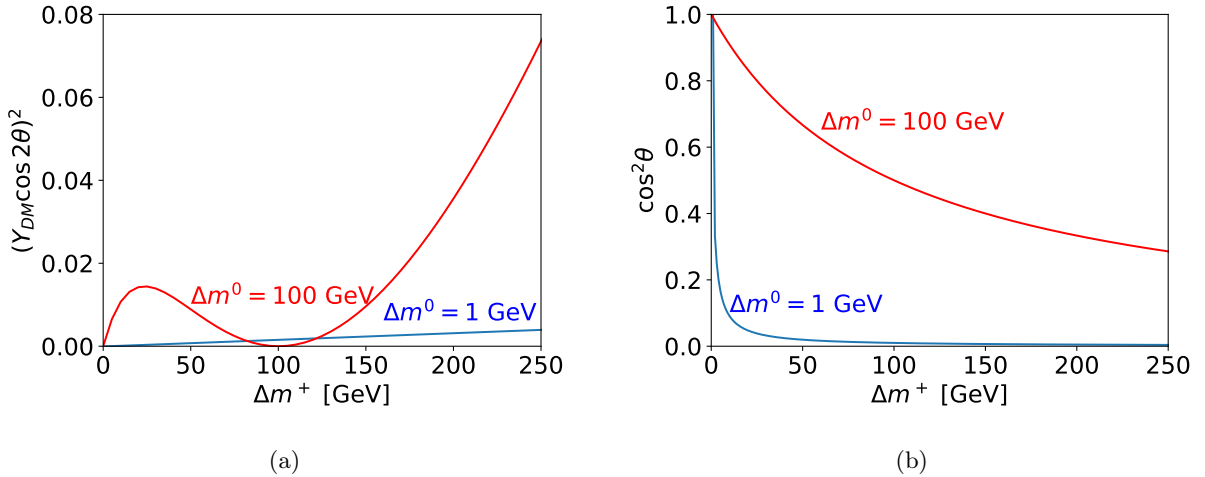


FIG. 4: $D_1 D_2 H$ coupling squared (a) and $\cos^2 \theta$ of the $\chi_1^0 - \chi_s^0$ mixing (b) as a function of Δm^+ for two values of $\Delta m^0 = 1$ GeV (blue) and 100 GeV (red).

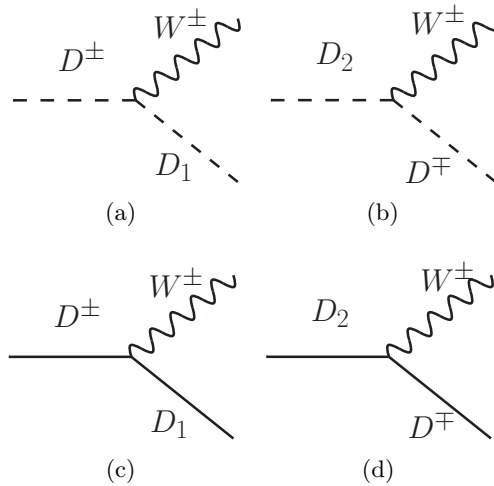


FIG. 5: Decays analogous between the i2HDM (left) and the MFDM model (right).

the i2HDM and MFDM model. In Fig. 6, we then present the unique decays of each model: the $D_2 \rightarrow Z D_1$ decay permitted in the i2HDM while the $D_2 \rightarrow H D_1$ and D' decays are so in the MFDM model.

The BRs for the decays leading to our DM signatures (see Figs. 5 and 6) are presented in Fig. 7 as a function of the Δm^+ parameter, again, for a 100 GeV DM mass and the two values of $\Delta m^0=1$ and 100 GeV. The D^\pm decay to W^\pm dominates in all cases. This is because, for the i2HDM, only $m_{D_2} > m_{D^\pm}$ is considered and so D^\pm can only decay to $W^\pm D_1$ while, for the MFDM model, D' and D^\pm are mass degenerate and their decay to one another is not permitted. For $\Delta m^0=1$, in the i2HDM (Fig. 7(a)), the D_2 decay to leptonically decaying Z and D_1 is favoured over the D_2 decay to leptonically decaying W^+ and D^- which is suppressed due to a small $D_2 - D^\pm$ mass splitting. This BR falls rapidly with increasing Δm^+ , due to D^+ in the final state increasing in mass, while the mass of the D_1 in the $D_2 \rightarrow Z D_1$ final state is fixed.

The behaviour of the D_2 BRs changes when considering $\Delta m^0 = 1 \rightarrow 100$ GeV (Fig. 7(b)) since

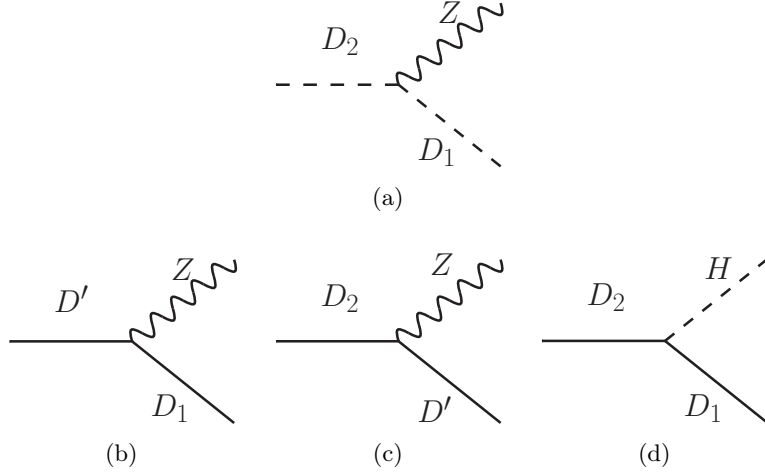


FIG. 6: Decays exclusive to the i2HDM (top) and MFDM model (bottom).

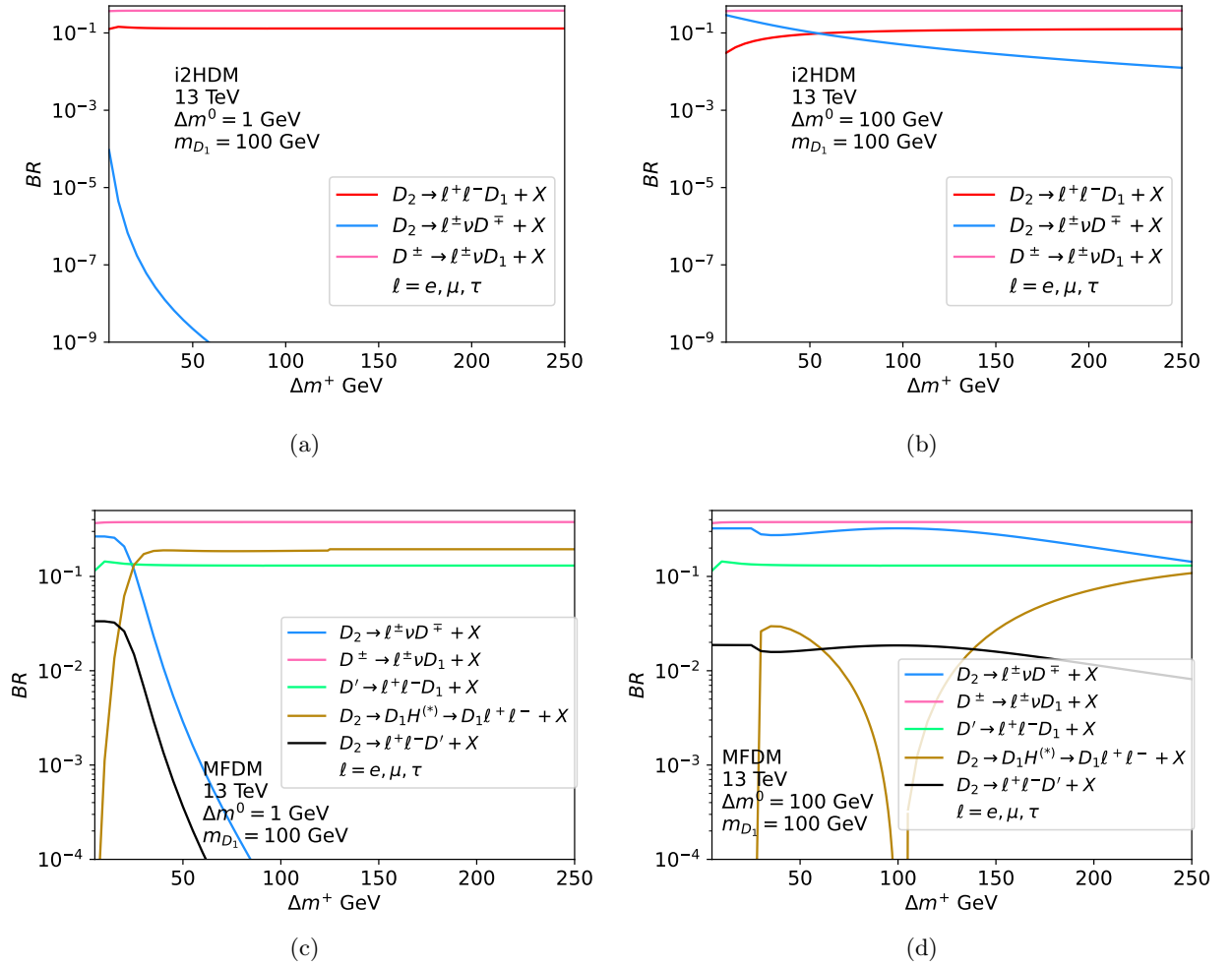


FIG. 7: The BRs of leptonic decays and DM particles for the i2HDM (top) and MFDM model (bottom) for $\Delta m^0 = 1$ and 100 GeV (left and right panels, respectively).

the $D_2 - D^\pm$ mass gap is increased, initially suppressing the D_2 decay to ZD_1 . However, the trend over increasing Δm^+ remains the same and the two D_2 BRs cross for Δm^+ around 60 GeV. Meanwhile, for the MFDM model, the $D' \rightarrow W^+D^-$ decay is not permitted and so the BR of the D' decay to a leptonically decaying Z and D_1 remains unchanged between Fig. 7(c) and (d).

The MFDM model decays from D_2 include a unique Higgs interaction, $D_2 \rightarrow D_1 H^{(*)}$, where the $D_2 D_1 H$ coupling is a product of the Yukawa Y_{DM} (which is proportional to $\sqrt{\Delta m^0 \Delta m^+}$) and $\cos(2\theta)$ of the $\chi_1^0 - \chi_s^0$ mixing angle θ . This interplay is seen in Fig. 4(a) (blue line), where Y_{DM} suppresses this coupling at small Δm^0 and Δm^+ , but the latter rises with increasing Δm^+ . For $\Delta m^0=1$ the shape of the $D_2 \rightarrow D_1 H^*$ (brown) line in Fig. 7(c) follows the trend just described, then it levels out as $\sqrt{\Delta m^+}$. As the Higgs boson becomes on-shell with increasing Δm^+ , a jump in the BR of leptonic decays via $D_2 \rightarrow D_1 H$ is observed in Fig. 7(c), due to the additional contribution $H \rightarrow W^+W^-$. Meanwhile, the D_2 decays to W^+D^- and ZD' are both controlled by the sine of the mixing angle, i.e., the amount by which the D_2 is χ_1^0 . Therefore, their shapes are similar to one another but the blue and black lines fall as the $D_2 \rightarrow D_1 H$ brown line increases with Δm^+ (note that the $D_2 \rightarrow W^+D^-$ BR is a factor ~ 8 larger than the $D_2 \rightarrow D'Z$ one due to combinatorics and the ratio m_Z/m_W).

Now, considering $\Delta m^0 = 100$ for the MFDM model, D_2 decays are strongly affected by any Δm^0 variation. In Fig. 7(d), $D_2 \rightarrow ZD'$ and $D_2 \rightarrow W^+D^-$ are now on-shell and these decays are then enhanced. When $\Delta m^+ = 30$ GeV and $m_{D_2} - m_{D_1} = 130$ GeV, the $D_2 \rightarrow HD_1$ decay (brown line) becomes on-shell and boosted, reducing the other D_2 decays proportionally. However, D_2 changes from mostly χ_s^0 to mostly χ_1^0 as Δm^+ reaches Δm^0 from below, where the coupling reaches zero at $\Delta m^+ = \Delta m^0 = 100$ GeV (see Fig. 4(a) red line). Beyond this value of Δm^+ , the coupling then increases with $\sqrt{\Delta m^+}$ as $\Delta m^+ > \Delta m^0$ which in turn reduces the $D_2 \rightarrow ZD'$ and $D_2 \rightarrow W^+D^-$ leptonic BRs above $\Delta m^+ > 100$ GeV as seen in Fig. 7(d).

The discussed combinations of production and decay rates provide the expected rates for the 2- and 3-lepton signatures which we study below at the (fast) detector level and compare to published LHC data.

IV. RESULTS

In order to understand the constraints on the models we study in this paper, we reinterpret existing multi-lepton searches at the LHC. We first provide a brief summary of the models, then describe briefly the reinterpretation tools for this work, finally followed by an assessment of the impact of these searches on our two benchmark models.

A. LHC Searches and Tools

We begin by identifying the LHC searches that can potentially be useful to constrain the latter. For the i2HDM, constraints were derived previously in [11] by reinterpreting 8 TeV 2- and 3-lepton searches using MadAnalysis5 [31]. In preparation for this publication, the previous work is verified using the public recast tool CheckMATE [18] (see Appendix A). The corresponding recast software is publicly available at [32, 33]. In this paper, we extend this result to 13 TeV for both the i2HDM and MFDM model based on searches available in CheckMATE.

In Tab. I, we identify the 13 TeV searches that are relevant for the reinterpretations in this paper. The most stringent constraints for these models are expected to emerge from LHC Supersymmetry searches targeting EW gauginos. Since we are investigating models with a variety of mass gaps in this paper, we look for searches that constrain both small and large mass gaps. We therefore note the following.

Analysis	Description	Final States	Lumi. [fb ⁻¹]
atlas_1609_01599 [34]	$t\bar{t}V$ cross-section measurement at 13 TeV	two or three leptons(one OSSF pair)+bjets	3.2
atlas_conf_2016_076 [35]	direct top squark pair + DM production	two leptons + jets + E_T^{miss}	13.3
atlas_conf_2016_096 [36]	EW production of charginos and neutralinos	two or three leptons + E_T^{miss}	13.3
atlas_1712_08119 [37]	EWinos search with soft leptons	two soft OSSF leptons + E_T^{miss}	36.1
cms_sus_16_039 [38]	EWinos in multilepton final state	\geq two leptons + τ + E_T^{miss}	35.9
cms_sus_16_025 [39]	EWino and stop compressed spectra	two soft OS leptons + E_T^{miss}	12.9
cms_sus_16_048 [40]	Search for new physics in events with soft leptons	two soft OS leptons + E_T^{miss}	35.9

TABLE I: The relevant 13 TeV ATLAS and CMS analyses which are sensitive to the DM signatures under study in this paper.

- For small mass gaps the CMS [41] soft lepton searches `cms_sus_16_025` [39] and `cms_sus_16_048` [40] can potentially constrain the parameter space under study here. The search `cms_sus_16_025` constrains $\chi_1^+ \chi_2^0$ pair production followed by decay to leptons and missing energy via off-shell W^\pm and Z bosons for mass gaps $\simeq 5 - 50$ GeV. It also constrains direct stop pair production followed by a decay to leptons via off-shell W^\pm 's for mass gaps up to 70 GeV. The search `cms_sus_16_048` targets the same EWino pair production as above and constrains mass gaps up to about 50 GeV at an integrated luminosity of 35.9 fb⁻¹. Both of the above searches require Opposite Sign (OS) $ee/\mu\mu/e\mu$ with leading leptons $p_T < 20$ GeV, $E_T^{\text{miss}} < 200$ GeV and at least one jet.
- For large mass gaps the ATLAS [16] search `atlas_conf_2016_096` [36] as well as the CMS search `cms_sus_16_039` [38] are the most constraining ones. These publications target EWino pair production with the same decay pattern as the soft lepton searches. The searches look for OS leptons and constrain mass gaps above 50 GeV.

The i2HDM and MFDM model input LHE files were produced with different mass parameters, as described in section III, with CalcHEP [26]. This is followed by showering and hadronisation using PYTHIA8 [29]. Jets, with final-state hadrons are constructed using FASTJET [42], while detector simulation is performed using DELPHES [30]. The entire process (barring parton level event generation) is performed within CheckMATE. The built-in AnalysisHandler processes the detector-level events with the user selected analyses. The signal size is determined based on the efficiency, acceptance, signal cross section and integrated luminosity [43] of the analysis.

B. Constraints on the i2HDM and MFDM Model

In this section, we present the results of our study for the i2HDM and MFDM model. For each of these scenarios, we constrain the parameter space in the $(m_{D_1}, \Delta m^+)$ plane using the searches quoted above to calculate the r -value:

$$r = \frac{S_{\text{DM}}}{S_{95}}, \quad (25)$$

where S_{DM} is the number of DM events expected to pass the signal selection and S_{95} is the 95% Confidence Level (CL) upper limit on the number of selected events. Any point with $r \geq 1$ is excluded by current LHC limits.

In general we observe the following.

- **Low Mass Gap: $2l + p_T^{\text{miss}}$ channel** - For low mass gaps the soft lepton analyses `cms_sus_16_025` and `cms_sus_16_048` constrain a large part of the parameter space in the

$2l + p_T^{\text{miss}}$ channel. For the MFDM model, they exclude phase space within $30 < m_{D_1} < 160$ GeV and $10 < \Delta m^+ < 50$ GeV for $\Delta m^0 = 1, 10, 100$ GeV. For the i2HDM, the two soft lepton analyses exclude phase space within $1 < m_{D_1} < 60$ GeV and $1 < \Delta m^+ < 60$ GeV for $\Delta m^0 = 1$ GeV as well as phase space within $1 < m_{D_1} < 40$ GeV and $1 < \Delta m^+ < 40$ GeV for $\Delta m^0 = 10, 100$ GeV.

- **Large Mass Gap: $2l + p_T^{\text{miss}}$ channel** - The harder 2-lepton signatures for the MFDM model are excluded by the `atlas_conf_2016_096` [36] signal regions 2LASF (2LADF) which require two same (different) flavours e/μ with $m_{ll} - m_Z > 10$ GeV and $m_{T2} > 0$ GeV. These signal regions exclude a phase space within $0 < m_{D_1} < 30$ GeV and $50 < \Delta m^+ < 80$ GeV for $\Delta m^0 = 1, 10, 100$ GeV. In the i2HDM case, the `atlas_conf_2016_096` analysis excludes a phase space within $0 < m_{D_1} < 45$ GeV and $60 < \Delta m^+ < 90$ GeV for $\Delta m^0 = 1, 10$ GeV.
- **$3l + p_T^{\text{miss}}$ channel** : For the MFDM model, the majority of the 3-lepton final state signal is excluded by the analysis `cms_sus_16_039` [38], by various signal regions, including SR_C03 ($150 < p_T^{\text{miss}} < 200$ GeV), SR_C04 ($200 < p_T^{\text{miss}} < 250$ GeV) and SR_C05 ($p_T^{\text{miss}} \geq 250$ GeV). They all require three leptons with at least two e or μ forming an opposite-sign same-flavour (OSSF) pair with $m_{ll} < 75$ GeV and including a τ -lepton. In the MFDM model, these signal regions exclude a phase space within $30 < m_{D_1} < 110$ GeV and $20 < \Delta m^+ < 300$ GeV for $\Delta m^0 = 1, 10, 100$ GeV. For the i2HDM, substantial r -value contributions are provided by the `cms_sus_16_039` analysis with signal regions for three leptons, SR_A30 (three leptons with one OSSF pair $75 < m_{ll} < 105$ GeV, $250 < p_T^{\text{miss}} < 400$ GeV), SR_K02 (four leptons, including two τ -leptons, $50 < p_T^{\text{miss}} < 100$ GeV), SR_F10 (three leptons including two τ -leptons) and SR_I03 (four or more leptons, including one τ), within the phase space $1 < m_{D_1} < 20$ GeV and $5 < \Delta m^+ < 70$ GeV for $\Delta m^0 = 1, 10$ GeV.

1. Constraints on the i2HDM channels

Using the re-parametrisation of Eq. (22), Fig. 8 (overlaid with total cross-section yields in Fig. 19 of Appendix D), show the r -value (see Eq. (25)) of the i2HDM 2- and 3-lepton signatures discussed in section III as a function of Δm^+ and m_{D_1} for various choices of Δm^0 . The 3-lepton contributions to the r -value are important, reaching up to $\sim 70\%$ of the 2-lepton-only r -values. However, 2-lepton-only r -values still dominate throughout the i2HDM contour plots.

For $\Delta m^0 = 1$ GeV, the dominant DM pair production process is $D_2 D_1$ (see Fig. 3(a)) and the dominant D_2 decay contribution is $D_2 \rightarrow Z D_1$ (see Fig. 7(a)), providing two leptons. The 3-lepton final states can be provided by the second largest DM production process, $D_2 D^\pm$, with decays as $D_2 \rightarrow Z D_1$ and $D^\pm \rightarrow W^\pm D_1$. This process and its decays can also fulfil the 2-lepton criteria if the W decays hadronically, or a lepton is misidentified.

The horizontal wedge of large r -value in Fig. 8(a) within $\Delta m^+ < 60$ GeV, $m_{D_1} < 70$ GeV is excluded by analyses `cms_sus_16_025` [39] and `cms_sus_16_048` [40], both with signal region SR1_weakino_1low_mll_2, requiring two leptons with $m_{ll} < 20$ GeV and at least one jet. In the i2HDM, this signature would be mostly provided by the leptonic Z decay and the hadronic W decay in the $D_2 D^\pm$ pair production. Most of this phase space is already excluded by LEP-II observations [44] (green line) and LEP-I limits from Z width measurements (grey line), excluding on-shell $Z \rightarrow D_2 D_1$ decays. However, at $\Delta m^+ < 8$ GeV, there is a small wedge of allowed phase space from soft leptons, when $m_{D_1} > 50$ GeV and $\Delta m^+ < 8$ GeV which is not covered by the LEP-I or LEP-II limits. The second, broader region of large r -value around $40 < \Delta m^+ < 100$ GeV is excluded by analysis `atlas_conf_2016_096` [36], signal region 2LASF. The dominant $D_2 D_1$ process with leptonic Z decay provides a signal that strongly contributes to the r -value in this region. Note

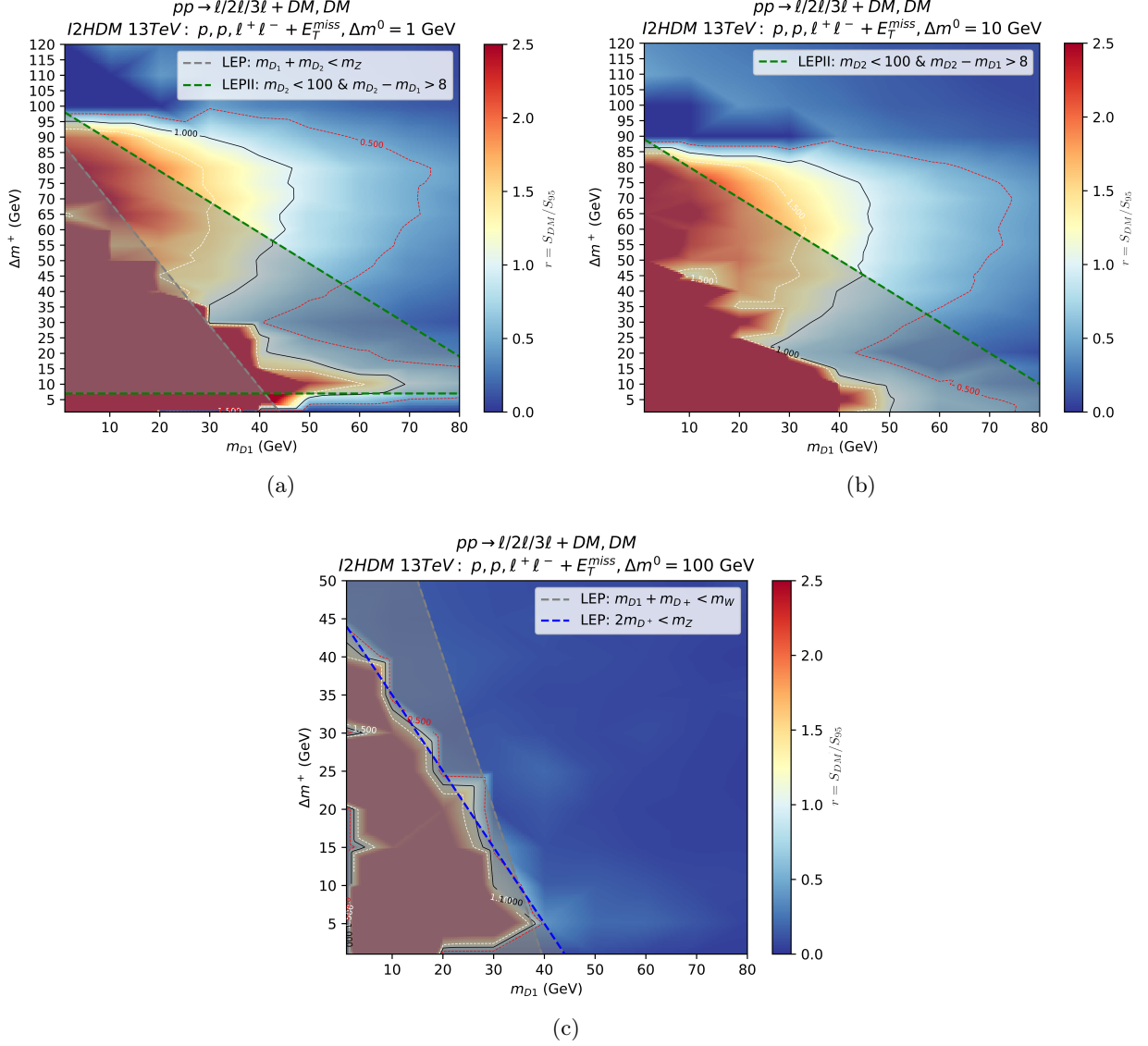


FIG. 8: i2HDM 13 TeV r -value contour plots for 2- and 3-lepton final states as a function of Δm^+ and m_{D1} for $\Delta m^0 = 1$ (a), $\Delta m^0 = 10$ (b) and $\Delta m^0 = 100$ (c) GeV. These are overlaid with limits from the LEP-I and LEP-II experiments [44], [45]. This includes $m_{D1} + m_{D2} < m_Z$ (grey line) and $2m_{D+} < m_Z$ (blue), from LEP-I Z boson width measurements excluding on-shell $Z \rightarrow D_1 D_2$ and $Z \rightarrow D^+ D^-$ decays. The same applies to the W width measurement excluding on-shell $W^\pm \rightarrow D^\pm D_1$ decays. The region $m_{D1} < 80$ GeV and $m_{D2} < 100$ GeV and $m_{D2} - m_{D1} > 8$ GeV (green lines) is excluded by LEP-II observations. Where these lines are absent, they are overlapped completely by the other LEP limits.

that a significant portion in Fig. 8(a) within the region $60 < \Delta m^+ < 95$ GeV and $m_{D1} < 50$ GeV not excluded by LEP, is excluded by these LHC limits.

Similar excluded regions are found for $\Delta m^0 = 10$ GeV in Fig. 8(b), but without the region of allowed phase space at small Δm^+ , for which the LEP-II limit now overlaps with this region (the grey line corresponding to the LEP limit $m_{D1} + m_{D2} < m_Z$ in Fig. 8(a) would be overlapped completely in Fig. 8(b) by the green line, so is not plotted here). Again, we see a significant

contribution from LHC limits in $60 < \Delta m^+ < 95$ GeV and $m_{D_1} < 50$ GeV where LEP does not already exclude.

As Δm^0 is increased further to 100 GeV in Fig. 8(c), the $D_2 D_1$ and $D_2 D^\pm$ cross sections are now suppressed at small Δm^+ (see Fig. 3(b)) compared to the dominant production $D^+ D^-$ for $\Delta m^+ < 130$ GeV, with decays $D^\pm \rightarrow W^\pm D_1$ (see Fig. 7(b)). The $M_{ll} > 100$ GeV cut applied in the `atlas_conf_2016_096` [36] analysis now removes all events for larger Δm^+ in Fig. 8(c), as heavier D_2 production cross section with harder lepton decays has decreased. In addition, the combination of LEP limits covers the totality of LHC limits for $\Delta m^0 = 100$ GeV in Fig. 8(c).

2. Constraints on the MFDM Model Channels

Based on the re-parametrisation of Eq. (10), Fig. 9 (overlaid in Fig. 20 of Appendix D with cross-section yields) shows the r -value exclusion contours of the MFDM model 2- and 3-lepton signatures discussed in section III as a function of Δm^+ and m_{D_1} for various choices of Δm^0 . The LEP-II limit in the MFDM model case corresponds to bounds on fermionic DM [45], which covers $m_{D^+} < 100$ GeV, a smaller Δm^+ range than the LEP limits for the i2HDM. Since we allow DM-Higgs coupling, the Higgs-to-invisible limit [46] of ~ 0.15 BR (magenta region) is also plotted.

Contributions to the 2-lepton r -value are provided by the dominant $D^+ D^-$ production (see Fig. 3(c)-(d)) with its leptonic decays $D^\pm \rightarrow W^\pm D_1$ (see Fig. 7(c)-(d)), by $D' D^\pm$ and, specifically for $\Delta m^0 = 1$ GeV, $D_2 D^\pm$ productions, where the latter two require D' and D_2 to decay leptonically. Cascades from $D' D_2$ production can also contribute to 2-lepton final states for $\Delta m^0 = 1$ GeV. However, $D_2 D^\pm$ and $D' D_2$ production become suppressed with $\Delta m^0 = 100$ GeV (see Fig. 3(d)). Meanwhile, $D' D_1$ production, which is suppressed for $\Delta m^0 = 1$ GeV, becomes enhanced with $\Delta m^0 = 100$ GeV as detailed in section III, contributing to 2-lepton final states. Contributions to the 3-lepton r -value are provided by the $D' D^\pm$ production with fully leptonic decays, although these are less likely to satisfy the signal regions that require τ -leptons than $D' D_2$ and $D_2 D^\pm$ production with $D_2 \rightarrow D_1 H^* \rightarrow D_1 \tau \tau$ decay. However, as stated, D_2 productions become suppressed with $\Delta m^0 = 100$ GeV (see Fig. 3(d)).

For $\Delta m^0 = 1$ GeV, the sharp excluded region of large r -value in Fig. 9(a) within $\Delta m^+ < 30$ GeV, $m_{D_1} < 150$ GeV was seen similarly for the i2HDM case in Fig. 8. As with the i2HDM case, this signal of soft leptons for the MFDM model in Fig. 9(a) is also excluded by the 2-lepton analyses `cms_sus_16_048` and `cms_sus_16_025` both with signal regions `stop_11low_pt`, `weakino_11low_mll`. These require two leptons and at least one jet, a signal also provided by the $D' D^\pm$ pair production, dominant here in the MFDM model (see Fig. 3(c)).

As Δm^+ increases, the 3-lepton r -value becomes larger than the 2-lepton-only r -value in the region $30 < \Delta m^+ < 100$ GeV and $m_{D_1} < 80$ GeV, excluded by the `cms_sus_16_039` [38] analysis signal regions requiring three leptons including τ . This is where the most dominant decay of D_3 changes from 1-lepton final states to 2-lepton final states including τ -leptons through virtual Higgs decays, as detailed in section III and Fig. 7(c). This gives more 3-lepton final states, with τ -leptons, from $D^+ D_2$ production. The additional third excluded area of smaller r -value than the previous two areas in Fig. 9(a), but still within an excluded region $120 < \Delta m^+ < 260$ GeV, $m_{D_1} < 100$ GeV has contributions to the signal from on-shell Higgs decay, where D_2 changes from decaying through H^* , into decaying to real Higgs which further decays to two W bosons or τ -leptons. This contributes more to the r -value as $\Delta m^+ > M_H$ for real Higgs production as detailed in section III. This region is also excluded by analysis `cms_sus_16_039` [38], with its 3-lepton (including one τ) signal regions.

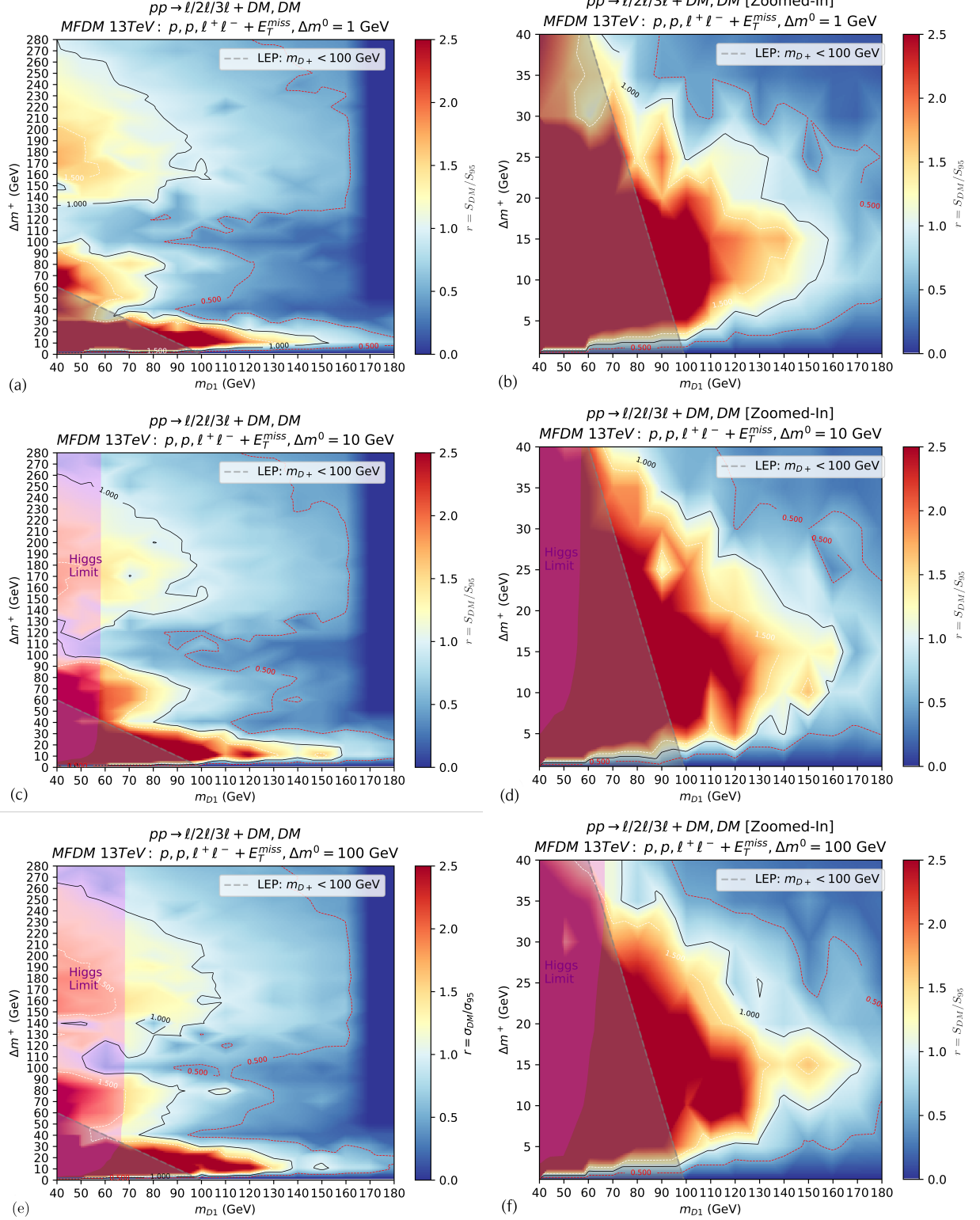


FIG. 9: MFDM 13 TeV r -value contours as a function of Δm^+ and m_{D1} for $\Delta m^0 = 1(a), 10(c), 100(e)$ GeV and zoomed in (b),(d),(f). The magenta region and grey region indicate the current Higgs-to-invisible limit [46] of 0.15 BR and LEP bounds on charginos for the fermionic DM case [45] respectively.

As Δm^0 is further increased to 10 GeV and 100 GeV in Fig. 9(b) and (c) respectively, the same r -value exclusion patterns are consistently observed. This no-lose theorem appears with the 2-lepton r -value due to the following scenarios: for small Δm^0 , the cross section is large for light D_2 production, but with suppressed coupling between $D_1 - D'$ (see Fig. 7(c)). Then, for large Δm^0 , this coupling is increased and (see Fig. 7(d)), while the heavy D_2 leads to suppressed production cross section.

For the 3-lepton r -value, while D_2 production becomes suppressed for increasing Δm^0 as shown in Fig. 3, its decays $D_2 \rightarrow W^+ D^-$ and $D_2 \rightarrow Z D'$ are enhanced, which can easily provide three leptons, including τ -leptons required by the relevant signal regions. In addition, $D' D^\pm$ production cross section is not affected by the Δm^0 variation.

As Δm^0 is increased, the Higgs-to-invisible limit [46] of ~ 0.15 BR excludes larger regions in Fig. 9(c)-(f), where $H \rightarrow D_1 D_1$ becomes the Higgs' dominant decay channel (since this coupling is proportional to Y_{DM}), until D_1 is too heavy to be produced on-shell. Other than this, the similarities in r -value plots for these three Δm^0 scenarios means we only need to consider the 2D plane $(\Delta m^+, m_{D_1})$. Fig. 10 visualises the relation of r -values and BR by superimposing the decay

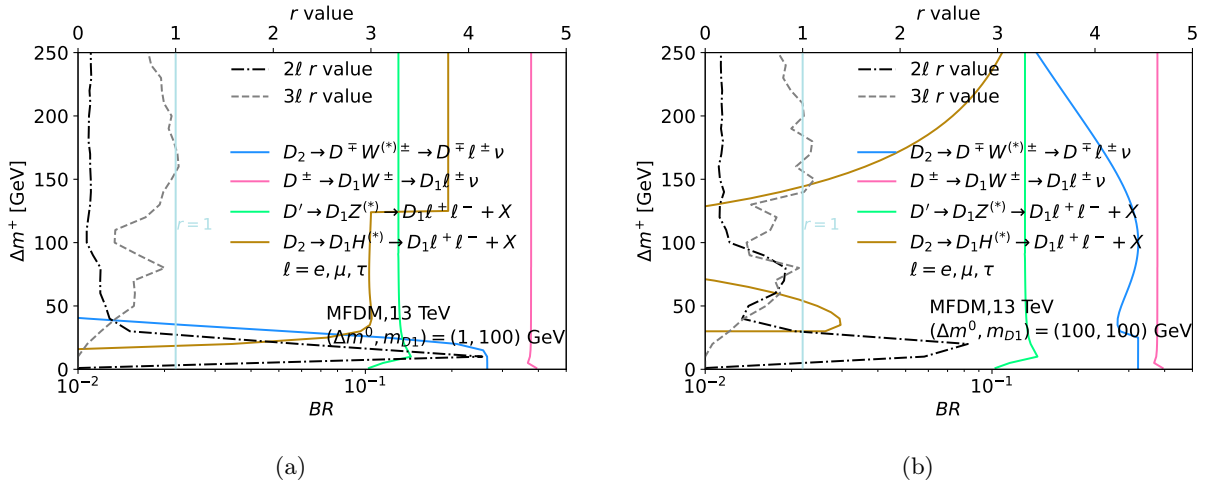


FIG. 10: Branching ratios (BR) as a function of the mass split Δm^+ for various MFDM decays, superimposed with the 2- and 3-lepton r -values, for $\Delta m^0 = 1$ GeV(a) and $\Delta m^0 = 100$ GeV(b). The DM mass is fixed to $m_{D_1} = 100$ GeV, corresponding to a vertical slice of Fig. 9(a) and (e).

BR from Fig. 7, rotated to match the contour plots in Fig. 9, with the 2-(dot-dashed line) and 3-(dashed line) lepton r -values from a vertical slice of Fig. 9 at $m_{D_1} = 100$ GeV as a function of Δm^+ .

For $\Delta m^0 = 1$ GeV (Fig. 10(a)), the dominant contribution to the r -value switches from 2-lepton final states to 3-lepton final states around $\Delta m^+ > 45$ GeV, due to the change in dominant branching of $D_2 \rightarrow D^\mp W^{*\pm} (\rightarrow \ell \nu)$ (blue line) to $D_2 \rightarrow D_1 H^* (\rightarrow \tau^+ \tau^-)$ (brown line) as Δm^+ (and m_{D_2}) increases. This corresponds to a phase space excluded specifically by the analysis cms_sus_16_039 [38], requiring three leptons with at least one τ -lepton, which can be provided in significant quantities by the H^* decay. Since the dominant productions at $\Delta m^0 = 1$ include $D_2 D^+$ and $D_2 D'$ (see Fig. 3(c)), the dominating contribution to the r -value changes from $D_2 D^+ \rightarrow \ell \nu D^+ \ell \nu D_1 + X$ (total of two charged leptons) to $D_2 D^+ \rightarrow \ell \ell D_1 \ell \nu D_1 + X$ and $D_2 D' \rightarrow \tau^+ \tau^- D_1 \ell \ell D_1$ (total of at least three charged leptons, including τ -leptons). As the Higgs boson becomes on-shell at $\Delta m^+ > 130$ GeV, the $H \rightarrow W^+ W^-$ channel opens, in addition to the real $H \rightarrow \tau^+ \tau^-$, noticeably contributing further to the 3-lepton r -value line in Fig. 10(a).

For $\Delta m^0 = 100$ GeV in Fig. 10(b), while D_2 production is suppressed (see Fig. 3(d)), the co-dominant pair production $D'D^\pm$ also provides three leptons via $D' \rightarrow D_1 Z$ (green line) and $D^\pm \rightarrow D_1 W^\pm$ (pink line). In addition, although D_2 production being suppressed, the D_2 decays $D_2 \rightarrow D^\pm W^\pm (\rightarrow l\nu)$ and $D_2 \rightarrow D' Z (\rightarrow ll)$ become strongly enhanced throughout (since W and Z are on-shell). Combined, they provide enough leptons, including τ -leptons, to compensate for the suppression of D_2 production and maintain a significant contribution to the 3-lepton r -value with increasing Δm^0 . As Δm^+ increases, an increase in the $D_2 \rightarrow D_1 H$ branching, which also decreases the $D_2 \rightarrow D^\pm W^\pm (\rightarrow l\nu)$ branching, contributes with τ -leptons to the 3-lepton r -value around $40 < \Delta m^+ < 60$ GeV. As detailed in section III, the $D_2 D_1 H$ coupling falls to zero again as Δm^+ reaches $\Delta m^0 = 100$ GeV where the mixing angle θ is such that $\cos(2\theta)$ and therefore the $D_2 D_1 H$ coupling falls to zero (see Fig. 4(a) red line). This decrease does not occur for the $\Delta m^0 = 1$ GeV case (see Fig. 4(a) blue line), since $\Delta m^+ > \Delta m^0$. However, this reduced contribution in Fig. 10(b) is compensated by the increase in $D_2 \rightarrow W^\pm D^\mp$ and $D_2 \rightarrow Z D'$. Finally, there is a boost in the 3-lepton r -value for $\Delta m^+ > 100$ GeV where the $D_2 D_1 H$ coupling becomes more enhanced.

C. Complementarity between the LHC and Non-collider Experiments

Finally we comment on the cosmological aspects of these models, first presenting relic density constraints on the i2HDM, then followed by relic density and direct detection constraints on the MFDM model.

The velocity-averaged annihilation cross section is dominated by DM scatterings to SM particles via the Z boson or the Higgs or via the quartic interaction $D_1 D_1 VV$. For the i2HDM, the relevant coupling that controls the annihilation cross section here is λ_{345} , described in section II. For the MFDM, instead the annihilation cross section is controlled by the Yukawa coupling Y_{DM} , Eq. (9) and the $D_2 - D_1$ mixing angle Eq. (6). Ignoring direct detection constraints, the i2HDM can account for the relic density in three distinct regions of parameter space [24]. The first is the so-called Higgs funnel region $m_{D_1} \simeq \frac{m_h}{2}$, the second around $m_{D_1} \simeq 72$ GeV and finally the heavy mass region $m_{D_1} \geq 500$ GeV. The Higgs funnel region is essentially a resonance annihilation regulated by the width and the coupling λ_{345} and constrains the coupling to $10^{-4} < \lambda_{345} < 10^{-2}$ if relic density has to be exactly satisfied. For the region around $m_{D_1} \simeq 72$ GeV, the annihilation proceeds primarily through the $D_1 D_1 VV$ quartic interaction, via a pure gauge coupling. As m_{D_1} approaches the WW mass threshold, this annihilation is over efficient, and results generically in under abundant dark matter. Finally, there is a region of parameter space with $m_{D_1} > 500$ GeV with destructive interference between the quartic interaction and a t-channel diagram involving heavier i2HDM states. Moving on to direct detection considerations, we realise that since DM-nucleon scattering cross section scales as λ_{345}^2 , almost all of the parameter space in the low mass region is highly constrained by Xenon100 [47] and XENON1T [48]. Note that the constraints on the invisible Higgs force the coupling $\lambda_{345} \leq 6 \times 10^{-3}$. Therefore the only viable region of parameter space consistent with relic density and direct detection constraints remaining corresponds to the Higgs funnel region.

In view of the above discussions, we set $\lambda_{345} \simeq 0$, such that the only region where relic density is satisfied is the high mass region via pure quartic gauge couplings. In principle the Higgs funnel region exists for non zero λ_{345} , and this region should be treated with caution. Meanwhile, for the MFDM model, DM scattering through the Z boson is suppressed due to a the $D_1 - D'$ mass split. Therefore in MFDM, direct detection constraints rely instead on DM scattering via Higgs exchange, which is proportional to the Yukawa coupling Y_{DM} (see Eq. (9)) and $D_2 - D_1$ mixing angle (see Eq. (6)).

We now present the results from Fig. 8 combined with the non-collider constraints on the i2HDM DM masses and mass splitting. Fig. 11 shows the excluded regions from relic density (RD: orange)

LEP (grey) and LHC limits (pink). The allowed regions include predicted DM that explains $<95\%$ of observed DM (blue) and DM that explains 95%-100% of observed DM (green).

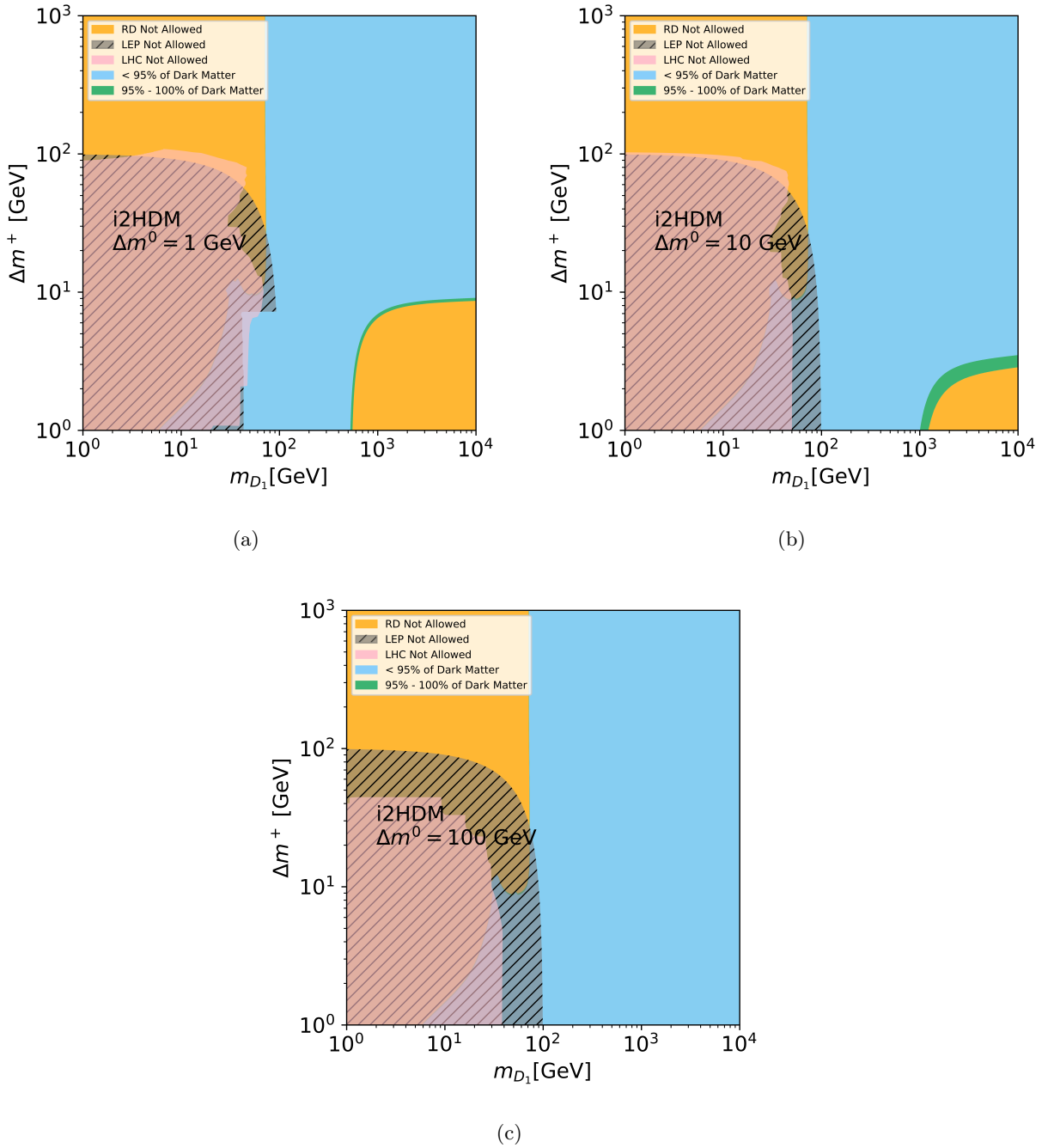


FIG. 11: LHC potential to exclude the i2HDM parameter space complementing relic density, LEP (hatched region)[44], [45] and LHC limits. Plots (a),(b) and (c) show regions for $\Delta m^+ = 1, 10, 100$ GeV respectively.

Since we assumed that $\lambda_{345} \sim 0$ in section II, the HD_1D_1 vertex necessary for DM scattering is not permitted and direct detection results therefore do not constrain this phase space for our scenario. As discussed in the context of Fig. 11, the LEP limits cover the majority of the LHC exclusion region, with the exception of a small region with $m_{D_1} > 40$ GeV, $2 < \Delta m^+ < 8$ GeV for $\Delta m^0 = 1$ GeV, and a region around $\Delta m^+ > 60$ GeV, $m_{D_1} < 50$ GeV for $\Delta m^0 = 1, 10$ GeV. The relic density limit excludes regions around $m_{D_1} < 70$ GeV before co-annihilation of $D_2 - D_1$ through Z and D^+D_1 through W^+ channels (proportional to the gauge weak coupling) open up, and $m_{D_1} > 600$ GeV, $\Delta m^+ < 9$ GeV for $\Delta m^0 = 1$ GeV. This second region then reduces to $m_{D_1} > 1000$ GeV, $\Delta m^+ < 3$ GeV for $\Delta m^0 = 10$ GeV and even further for $\Delta m^0 = 100$ GeV. For large DM mass but small mass split, the relic density remains too large for relic density constraints. However, for large DM masses and mass split, direct annihilation through WW and ZZ opens, dropping the relic density.

In Fig. 12, we now present the results from Fig. 9 combined with the non-collider constraints on the MFDM model DM masses and mass splitting. Again, the allowed regions include predicted DM that explains $<95\%$ of observed DM (blue) and DM that explains $95\%-100\%$ of observed DM (green). Relic density (orange), LEP limits (grey) and LHC limits (pink) are also displayed presented in Fig. 12. For the MFDM model we now include regions excluded from direct detection (DD: red) since we allow D_1D_1H interactions for this model. As discussed in the context of Fig. 9, the new LHC limits extend the phase-space coverage significantly beyond the LEP limits, including a substantial portion of the Higgs-funnel region around $m_{D_1} = 60$ GeV.

The direct detection exclusion region from XENON1T [48] limits an increasing range of Δm^+ with increasing Δm^0 as Yukawa coupling Y_{DM} (see Eq. (9)) increases, since direct detection in the MFDM model comes from DM scattering with Higgs. This is approximately within the region $\Delta m^+ > 10$ GeV and $m_{D_1} < 350$ GeV for $\Delta m^0 = 1$ GeV in Fig. 12(a) and $\Delta m^+ > 6$ GeV, for $\Delta m^0 = 10$ GeV in Fig. 12(b). However, when Δm^0 is sufficiently large (Fig. 12(c)) there is little change in this exclusion region, above $\Delta m^+ > 6$ GeV, as the Y_{DM} coupling relevant for direct detection converges towards $\sqrt{\Delta m^0}$.

In the region of $m_{D_1} > 800$ GeV the relic density excludes a larger range of m_{D_1} with increasing Δm^+ as the DM co-annihilation of DD^+ through W and of D_1D' through Z becomes suppressed, enhancing the relic density above the exclusion limit for smaller values of m_{D_1} . However, starting with $m_{D_1} = 100$ GeV, as the DM mass increases, the region of excluded Δm^+ decreases due to an enhancement of the $D_1D^-W^+$ and $D_1D'Z$ couplings proportional to $\cos\theta$. The same couplings are relevant for DM self-annihilation through D^\pm to W^+W^- or through D' to ZZ respectively. This trend continues until the required relic density is too high as $m_{D_1} > 300$ GeV, for which less DM annihilation suppression is needed. This happens roughly within the regions $m_{D_1} > 600$ GeV, $\Delta m^+ < 15$ GeV and $m_{D_1} > 80$ GeV $\Delta m^+ > 15$ GeV for $\Delta m^0 = 1$ GeV in Fig. 12(a). Then, for $\Delta m^0 = 10$ GeV, the lower limit for $m_{D_1} < 600$ GeV increases to $\Delta m^+ > 20$ GeV, and the limit for smaller $\Delta m^+ < 10$ GeV changes to $m_{D_1} > 900$ GeV in Fig. 12(b). This excluded space reduces further for $\Delta m^0 = 100$ GeV in Fig. 12(c) to $m_{D_1} > 1050$ GeV within $\Delta m^+ < 30$ GeV. This effect is due to increasing Δm^0 and is attributed to an enhancement of the DM co-annihilation of DD^+ through W and of D_1D' through Z , with couplings proportional to $\cos\theta$ (see Fig. 4(b)).

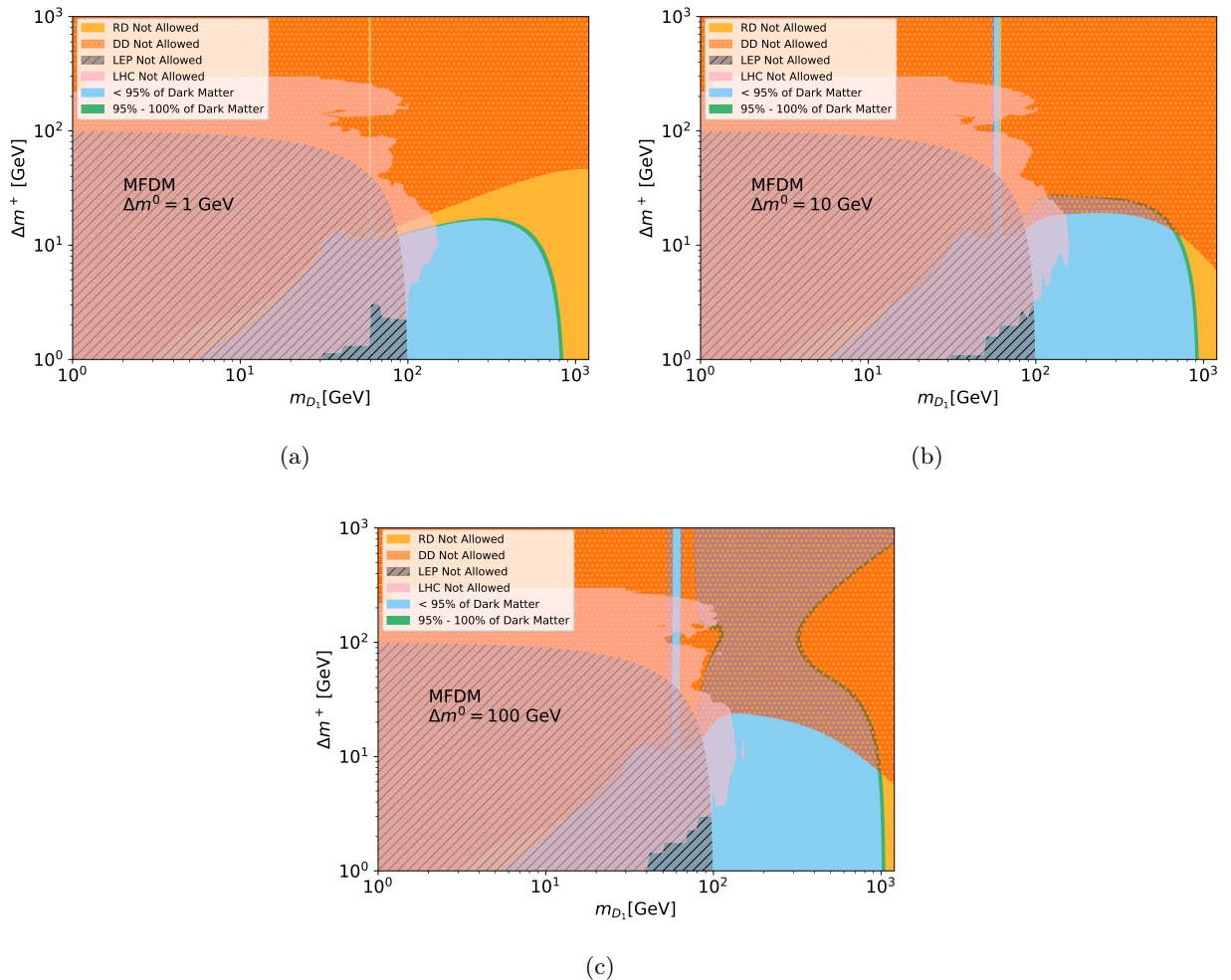


FIG. 12: LHC potential to exclude the MFDM model parameter space complementing non-collider constraints direct detection, relic density, LEP (hatched region)[45] and LHC limits. Plots (a),(b) and (c) show regions for $\Delta m^+ = 1, 10, 100$ GeV respectively.

V. CONCLUSIONS

In this paper, we have explored the full parameter space relevant to 2- and 3-lepton signatures at the LHC emerging from two representative minimal consistent scenarios with scalar and fermion DM: the i2HDM and MFDM model, respectively. In our analysis, we have suggested a new parametrisation for both frameworks in terms of the DM mass, m_{D_1} , the mass difference between it and its charged multiplet partner, $\Delta m^+ = m_{D^+} - m_{D_1}$, as well as the mass difference between D^+ and D_2 (the next-to-lightest neutral Z_2 -odd particle), $\Delta m^0 = m_{D_2} - m_{D^+}$. This parametrisation allowed us to understand and interpret better the properties of the models under study and visualise a no-lose theorem covering their full parameter spaces. This approach is generic and quite model-independent since the mentioned mass differences are related to the couplings of the DM particle to the SM sector.

Our numerical results have led to the newest and most up-to-date LHC limits on the i2HDM and MFDM model parameter spaces, coming from the complementary combination of the afore-

mentioned 2- and 3-lepton signatures. In particular, in the case of the i2HDM, we have found new regions which the LHC can cover above the LEP limits, for example: a) for a small $\Delta m^0 \lesssim 1$ GeV, the LHC excludes regions with $45 \text{ GeV} \lesssim m_{D1} \lesssim 55 \text{ GeV}$ and $\Delta m^+ \lesssim 8 \text{ GeV}$ as well as with $10 \text{ GeV} \lesssim m_{D1} \lesssim 50 \text{ GeV}$ and $60 \text{ GeV} \lesssim \Delta m^+ \lesssim 95 \text{ GeV}$; b) for a larger $\Delta m^0 \simeq 10$ GeV, the LHC excludes regions with $10 \text{ GeV} \lesssim m_{D1} \lesssim 50 \text{ GeV}$ and $50 \text{ GeV} \lesssim \Delta m^+ \lesssim 85 \text{ GeV}$. Furthermore, in the case of the MFDM model, the LHC probes a notably larger DM parameter space, in comparison, for example: a) for $\Delta m^+ \simeq 10$ GeV, the LHC excludes DM masses up to 150–160 GeV, hence, going well beyond not only the LEP limits but also the LHC ones in mono-jet; b) for a much larger $\Delta m^+ \simeq 150 - 200$ GeV, the LHC excludes DM masses up to 100 GeV, which is also well beyond such LEP and LHC constraints. Therefore, the parametrisation that we have suggested thus allows one to clearly establish a no-lose theorem for the MFDM model parameter space: the increase of Δm^0 leads to the increase of the $W^\mp D_1 D^\pm$ coupling and respective increase of the $D_1 D^\pm$ production rate while kinematically suppressing the $D_2 D^\pm$ production rate. These two trends roughly compensate each other making the exclusion picture in the $(m_{D1}, \Delta m^+)$ plane quasi-independent of Δm^0 .

We have also found another important complementarity between the 2- and 3-lepton signatures. The first one mainly covers low values of Δm^+ while the second one is enhanced in the region of large Δm^+ values. To corroborate our quantitative results, we have implemented and validated a 8 TeV ATLAS multi-lepton analysis into the CheckMATE package and made available this analysis publicly to the community. We have then created a map of the LHC efficiencies and cross-section limits for such 2- and 3-lepton signatures for the simple parametrisation of the parameter space that we have suggested, which would then allow for a quick and easy model-independent reinterpretation of the LHC limits for analogous classes of models.

Finally, we have produced combined constraints from the LHC, DM relic density and DM direct search experiments delineating the current status of the i2HDM and MFDM model parameter spaces. These combined limits indicate yet another important complementarity, the one between non-collider experiments and the LHC, both of which will continue to probe unknown territory of DM parameter space, hopefully resulting in a DM signal discovery. In such a quest, we deem the multi-lepton signatures studied here to be of the utmost importance at the LHC.

ACKNOWLEDGEMENTS

AB and SM acknowledge support from the STFC Consolidated Grant ST/L000296/1 and are partially financed through the NExT Institute. AB also acknowledges support from a Soton-FAPESP grant. All authors acknowledge the use of the IRIDIS High-Performance Computing Facility and associated support services at the University of Southampton in completing this work.

Appendix A: 8 TeV Validation: i2HDM

Appendix A details the validation of our CheckMATE recast for 8 TeV LHC exclusion limits for 2-lepton final states by comparing with the existing MadAnalysis implementation [49]. The CheckMATE analysis code was written based on and validated with the original experimental results, which searched for direct production of charginos, neutralinos and sleptons in final states with two leptons and missing transverse momentum [50] at the LHC. This was implemented using the CheckMATE's AnalysisManager in the current public build, and the SUSY analysis is available at [32]. The cutflows are given in tables II and III.

Global Cut	
E_T^{miss}	> 0 GeV
Base leptons	2
e^+e^- trigger	97%
$\mu^+\mu^-$ trigger	89%
$e\mu$ trigger	75%
Signal leptons	2
Leading lepton p_T	> 35 GeV
sub-leading lepton p_T	> 20 GeV
$M_{\ell\ell}$	> 20 GeV
jets	0
$ M_{\ell\ell} - M_Z $	> 10 GeV

TABLE II: Cutflow for all events in the 8 TeV ATLAS SUSY analysis for 2-lepton+ E_T^{miss} finals states, implemented in CheckMATE.

SR	m_{T2}^{90}	m_{T2}^{120}	m_{T2}^{150}	WWa	WWb	WWc	Zjets
$M_{\ell\ell}$				< 120	< 170		
$p_T(\ell\ell)$				> 80			> 80
$E_T^{miss,rel}$				> 80			> 80
m_{T2}	> 90	> 120	> 150		> 90	> 100	

TABLE III: Cutflows used for the specific signal regions in the 8 TeV ATLAS SUSY analysis for 2-lepton+ E_T^{miss} finals states, implemented in CheckMATE.

The 8 TeV ATLAS analysis searching for invisible decays of a Higgs boson produced in association with Z [50], previously recasted for MadAnalysis [51] was also written for the CheckMATE analysis performed here, as it also looks for final states with two leptons and missing energy. The public code of the Higgs analysis is available at [33]. The cutflow is given in table IV.

The events used for the validations were generated with CalcHEP, with 100000 events produced for each 9 benchmark points, using the SLHA files provided from HepData[52] and 1 benchmark point for $HZ \rightarrow$ invisible, with $M_H = 125.5$ GeV. Leptonic decays of Z in the HZ production, $\chi^\pm\chi^0$ production and W in the $\chi^+\chi^-$, were also specified in CalcHEP to improve efficiency, which were then showered with CheckMATE's built-in PYTHIA8 module. Detector effects are also applied via CheckMATE with a DELPHES module. Validation for the SUSY analysis is available at [53] and Higgs analysis available at [54].

The motivation behind fixing m_{D^+} is because it is mostly only important for D^+D^- production, which give an additional EW coupling factor compared to D_2D_1 production, only providing

Global Cut	
Base leptons	2
Lepton p_T	> 20 GeV
Z-window	$76 < M_{\ell\ell} < 106$ GeV
E_T^{miss}	> 90 GeV
$d\phi(E_T^{miss}, p_T^{miss})$	< 0.2
$\Delta\phi(p_T(\ell\ell), E_T^{miss})$	> 2.6
$\Delta\phi(\ell, \ell)$	< 1.7
$ \frac{E_T^{miss} - p_T(\ell\ell)}{p_T(\ell\ell)} $	> 0.2
jets	0

TABLE IV: Cutflow for all events in the 8 TeV ATLAS Higgs analysis for 2-lepton+ E_T^{miss} final states, implemented in CheckMATE.

significant contributions to r -value at very light m_{D+} . The ZD_1D_1 production is also less dominant as the ZZD_1D_1 coupling is quadratic and therefore weak compared to other couplings. The lowest allowed LEP limit of $m_{D+} = 85$ GeV is used and the higher value of $m_{D+} = 150$ GeV for comparison.

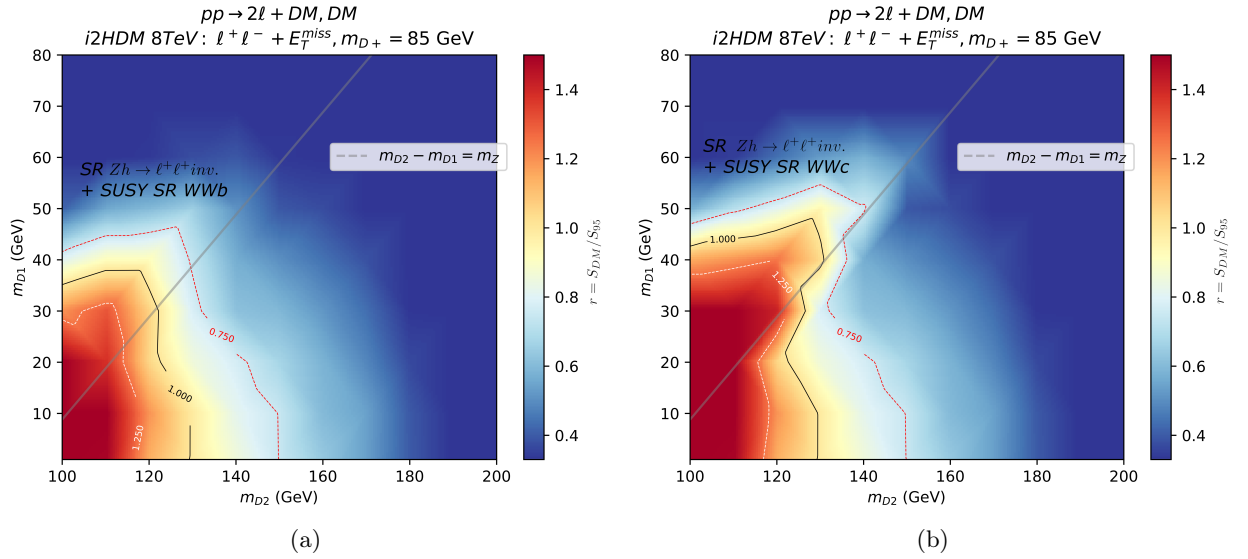


FIG. 13: r -value Exclusion plots as a function of m_{D_2} in i2HDM at 8 TeV, $m_{D+} = 85$ GeV, signal regions WWb +Higgs (a) and WWc +Higgs (b).

The r -value contour plots for $m_{D+} = 85$ GeV in Fig. 13(a) for the WWb signal region shows that the Run 1 ATLAS 2-lepton analysis excludes for the lightest DM mass of $m_{D_1} \leq 35$ GeV for $m_{D_2} = 100$ GeV, reaching a maximum of ~ 40 GeV as m_{D_2} is increased. In the case of Fig. 13(b), the WWc signal region reports stronger limits, excluding the lightest DM mass of $m_{D_1} \leq 40$ GeV for $m_{D_2} = 100$ GeV, reaching a maximum of ~ 45 GeV as m_{D_2} is increased. For $m_{D_1} \rightarrow 0$, both cases exclude up to a mass of $m_{D_2} = 130$ GeV.

By increasing m_{D+} to 150 GeV in Fig. 14(a), the WWb signal region excludes up to $m_{D_1} = 35$ GeV at $m_{D_2} = 100$ GeV, to $m_{D_1} = 40$ GeV with increasing m_{D_2} . In comparison, the WWc signal region excludes masses from $m_{D_1} = 40$ GeV at $m_{D_2} = 100$ GeV, to $m_{D_1} = 50$ GeV as m_{D_2} is

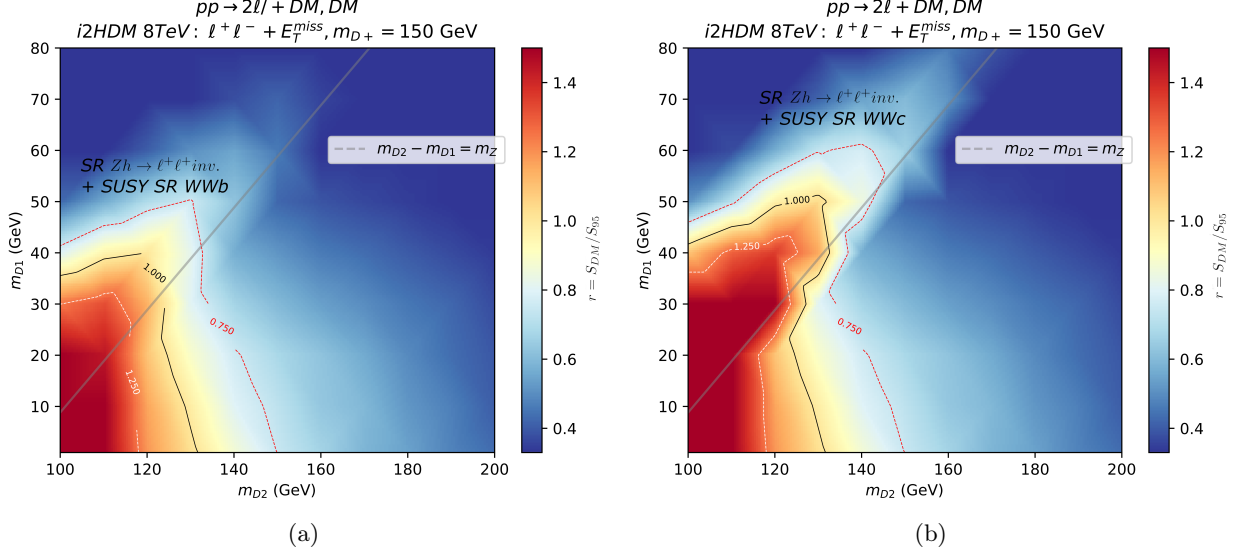


FIG. 14: r -value exclusion plots as a function of m_{D_2} in i2HDM for 8 TeV, $m_{D_+} = 150$ GeV, signal regions WWb +Higgs (a) and WWc +Higgs (b).

increased.

Constraints increase with larger m_{D_+} in both WWb and WWc signal regions, due to increased contributions from D^+D^- production and from D_2D^+ production.

For larger m_{D_2} , the signal events coming from D_2D_1 production is smaller as the Z decay from D_2 is replaced in favour of W decay to D^+ and its decay to an additional W^+ and D_1 , which produces much softer leptons than required by the signal region cuts.

As m_{D_2} is increased, m_{D_1} is further constrained when considering the phase space above $m_{D_2} - m_{D_1} = m_Z$, due to harder lepton production Z decaying from D_2 . Beyond this line, for a large enough $m_{D_2} - m_{D_1}$ mass splitting, the Z -veto required by the SUSY analysis is no longer fulfilled by the signal, as real Z decay emerges in the production. Instead, the Z -window required by the Higgs analysis accepts these events, and becomes the dominant signal region as the mass splitting is further increased, independent of m_{D_+} .

From Fig. 13(a) and 14(a) the WWb +Higgs analyses agree with the general shape in [17] Fig. 1, for both $m_{D_+} = 85$ GeV and 150 GeV, but with lower r -value overall. However, results with larger r -value are obtained when considering WWc +Higgs signal regions in Fig. 13(b) and 14(b). While [17] considered both WWb and the $HZ \rightarrow$ invisible, they did not consider the WWc signal region. This is because, although the WWc signal region gives a larger observed r value than WWb , the expected r value is lower than WWb (deeming it the better channel by analysis tools). It is worth noting that the MadAnalysis validation for this signal region is overestimated compared to the experimental paper by a small amount, while the CheckMATE analysis implemented is closer to the experimental findings for survived number of MC events. contour exclusion limits for WWc , where a higher m_{T2} cut on the leptons is implemented, shows higher observed r -value than the original paper's WWb contour exclusion limits.

Appendix B: i2HDM 13 TeV, 2- or 3-lepton Final states

In appendixB the analysis in [17] is then extended to higher centre of mass energies, using all available ATLAS and CMS 13 TeV analyses in CheckMATE. There is no equivalent to the Higgs $ZH \rightarrow \ell^+\ell^- + \text{invisible}$ recasted code as of writing, which is why the r -value beyond the $m_{D_2} - m_{D_1} = m_Z$ line is negligible.

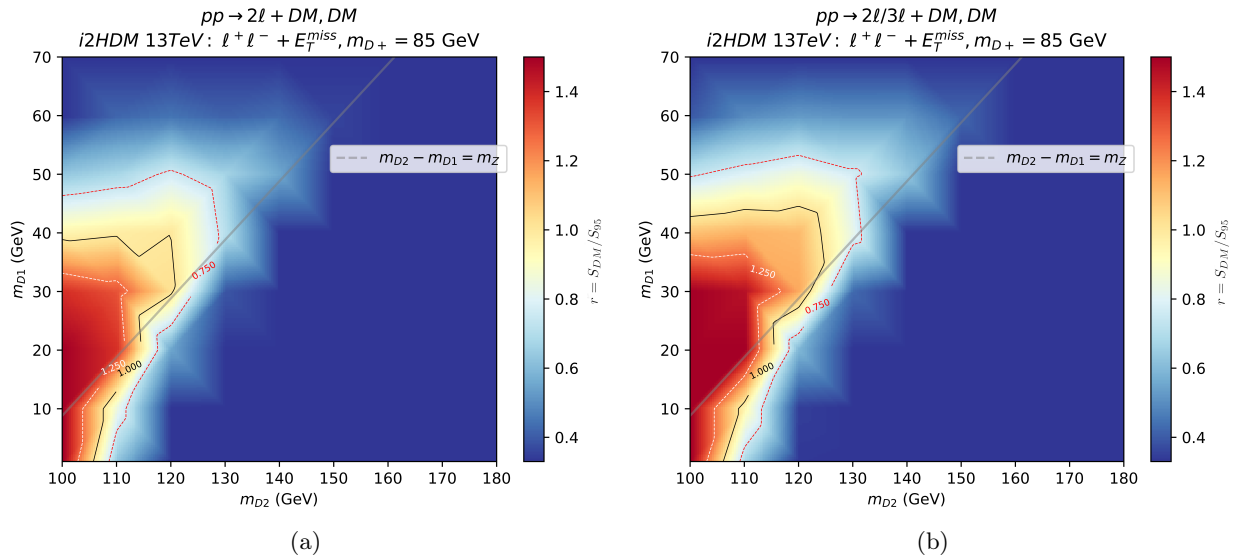


FIG. 15: r -value exclusion plots in i2HDM for 13 TeV, $m_{D^+} = 85$ GeV, using signal regions with the highest r -values for two leptons (a) and 2- or 3-lepton (b) final states.

Extended to 13 TeV, Fig. 15 shows that this does not necessarily improve results, due to scaling of vector boson backgrounds in this phase space. Also shown between Fig. 15(a) and (b) is the improvement to r -value due to the inclusion of 3-lepton final states. This introduces 6 additional contributing diagrams where D_2, D^+ production (a) plays an important role. D_2 provides two leptons via $D_2 \rightarrow Z(\ell^+\ell^-)$, D_1 and D^+ gives one extra lepton via $D^+ \rightarrow W^+(\ell^+\nu)$, D_1 which contributes in heavier D_1 (and thus softer leptons) phase spaces than 2-lepton exclusive searches.

If D^+ is heavy enough, it can decay via D_2 , but this only occurs in Fig 16. The m_{D_1} extends from 40 GeV to 45 GeV limit, while m_{D_2} can extend from 120 GeV to 125 GeV.

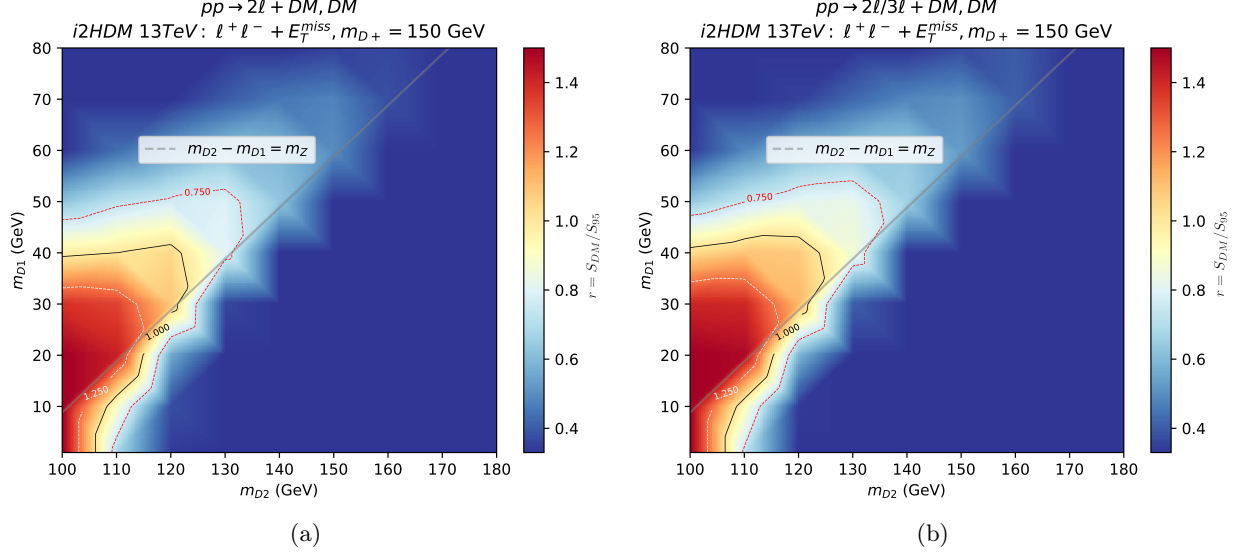


FIG. 16: r -value exclusion plots in $i2HDM$ for 13 TeV, $m_{D+} = 150$ GeV, using signal regions with the highest r -values for two leptons (a) and 2- or 3-lepton (b) final states.

Shown in Fig. 16 is the improvement from increasing lepton multiplicity for the larger m_{D+} value. Although less apparent than in Fig. 15, there are extensions to exclusion limits from under $m_{D1} = 40$ GeV to above the 40 GeV line and similarly small extensions to the m_{D2} limit.

The diagrams with three leptons in the final state can now contribute to the relevant phase space, but as this chain of decays contains more steps than other contributions, the soft leptons it produces mostly do not pass the cuts here. Contrary to the 8 TeV case, there is not much increase in limits when moving to heavier D_2 . In fact, for 2- and 3-lepton searches, Fig. 15(b) has limits of $m_{D1} = 44 - 45$ GeV for $m_{D2} = 100$ GeV, while for $m_{D+} = 150$ GeV figure 16(b) only has limits reaching $m_{D1} = 40 - 41$ GeV due to more processes that do not necessarily fulfil the signal criteria.

In principle one would combine 13 TeV result with the 8 TeV exclusion limits for a comprehensive picture of LHC limits. Although 8 TeV limits are stronger than 13 TeV limits for the phase space in [17] and in this appendix, 8 TeV results do not improve within the phase space of our 13 TeV results in new parametrisation, shown in section IV.

Appendix C: MFDM 8 TeV

In appendix C 8 TeV r -value contour plots for MFDM are next discussed, starting with the same 8 TeV analyses that were used in the i2HDM case.

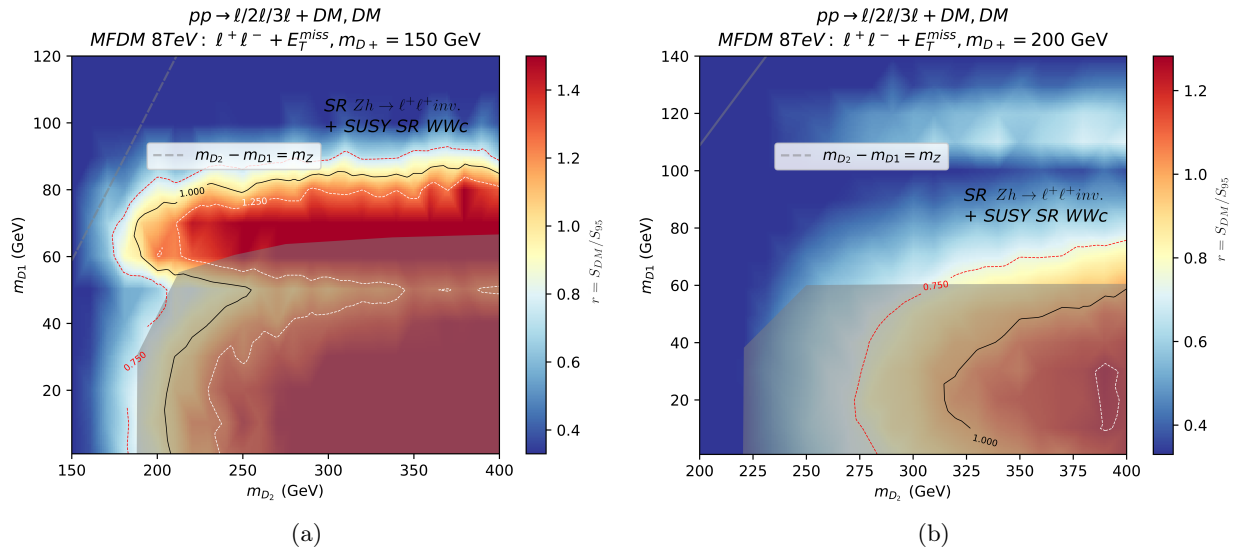


FIG. 17: The r -value exclusion plots in MFDM for 8 TeV, $m_{D+} = 150$ GeV (a) and $m_{D+} = 200$ GeV (b), from the signal regions WWc +Higgs.

Plots in Fig. 17 show fixed m_{D+} results, with scans in the m_{D_1} - m_{D_2} plane. The shaded region shows the Higgs to invisible excluded region, covering a large phase space of the CheckMATE excluded region. In figure 17(a), where $m_{D+} = 150$ GeV, the region above $m_{D_1} = 60$ GeV has limits reaching to $m_{D_1} < 85$ GeV excluded while $m_{D_2} > 180$ excluded. As m_{D_2} increases, this increases the split between D_2 and D^+/D' , increasing the Yukawa coupling in Eq. (9). This facilitates more decays that would lead to leptonic final states, thus r -value is increased in the positive x-axis direction. In the y-axis, as DM mass is increased, the exclusion changes from `atlas_higgs_2013_03` analysis at low DM mass, to the `atlas_1403_5294` analysis at higher DM mass. Looking at Tables II, IV, this is due to the Z-window changing to a Z-veto with softer leptons being produced in association with harder DM for the same input energy.

Fig. 17(b) shows $m_{D+} = 200$ GeV, where no exclusion outside of the Higgs to invisible limit of $m_{D_1} < 60$ GeV excluded for $m_{D_2} > 220$ GeV. This is because m_{D+} and $m_{D'}$ become too heavy to produce at these masses, so the sources of leptonic final states are suppressed.

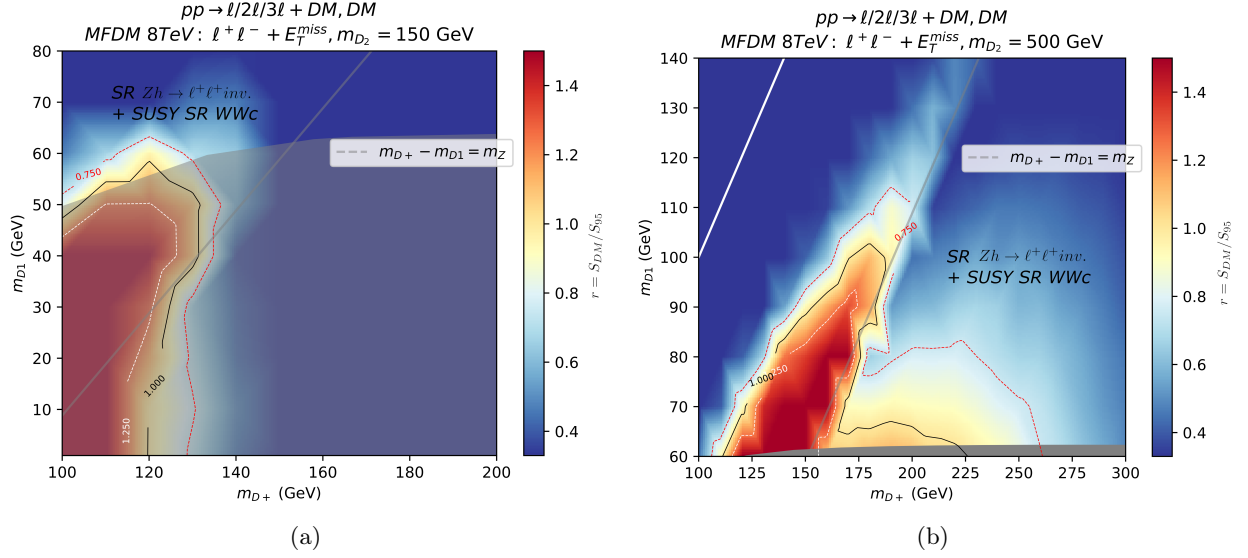


FIG. 18: r -value exclusion plots in MFDM for 8 TeV, $m_{D_2} = 150$ GeV (a), $m_{D_2} = 500$ GeV (b) from signal regions WWc +Higgs.

The plots in Fig. 18 for MFDM at 8 TeV with fixed m_{D_2} , showing the m_{D_1} - m_{D_+} plane, are more analogous to those displayed for the i2HDM results shown previously. Figure 18(a) with $m_{D_2} = 150$ GeV is mostly excluded by Higgs to invisible limits, of $m_{D_1} < 60$ GeV excluded.

On the other hand, Fig. 18(b) limits, for $m_{D_2} = 500$ GeV, extend much further. It excludes a peak at $m_{D_1} = 100$ GeV, $m_{D_+} = 180$ GeV, and follows along M_Z in terms of the mass split between m_{D_+} and m_{D_1} . This is when D' can decay via real Z boson to two leptons, and D_1 in the final state. It is also close to when this mass split equals M_W , facilitating two D^\pm decays via real W^\pm to a charged lepton and neutrino, along with D_1 in the final state.

In Fig. 18(b) there is an additional region of large r -value at $160 \text{ GeV} < m_{D_+} < 225 \text{ GeV}$, with a limit of $m_{D_1} = 65$ GeV excluded, coming from the atlas_higgs_2013_03 analysis with harder leptonic decays, and lighter D_1 .

Appendix D: Numerical Overlaid Plots

In appendix D we present the exclusion plots overlaid with cross sections in fb for 2 or 3-leptonic final states. We first present the results for i2HDM in Fig.19 and MFDM in Fig.20.

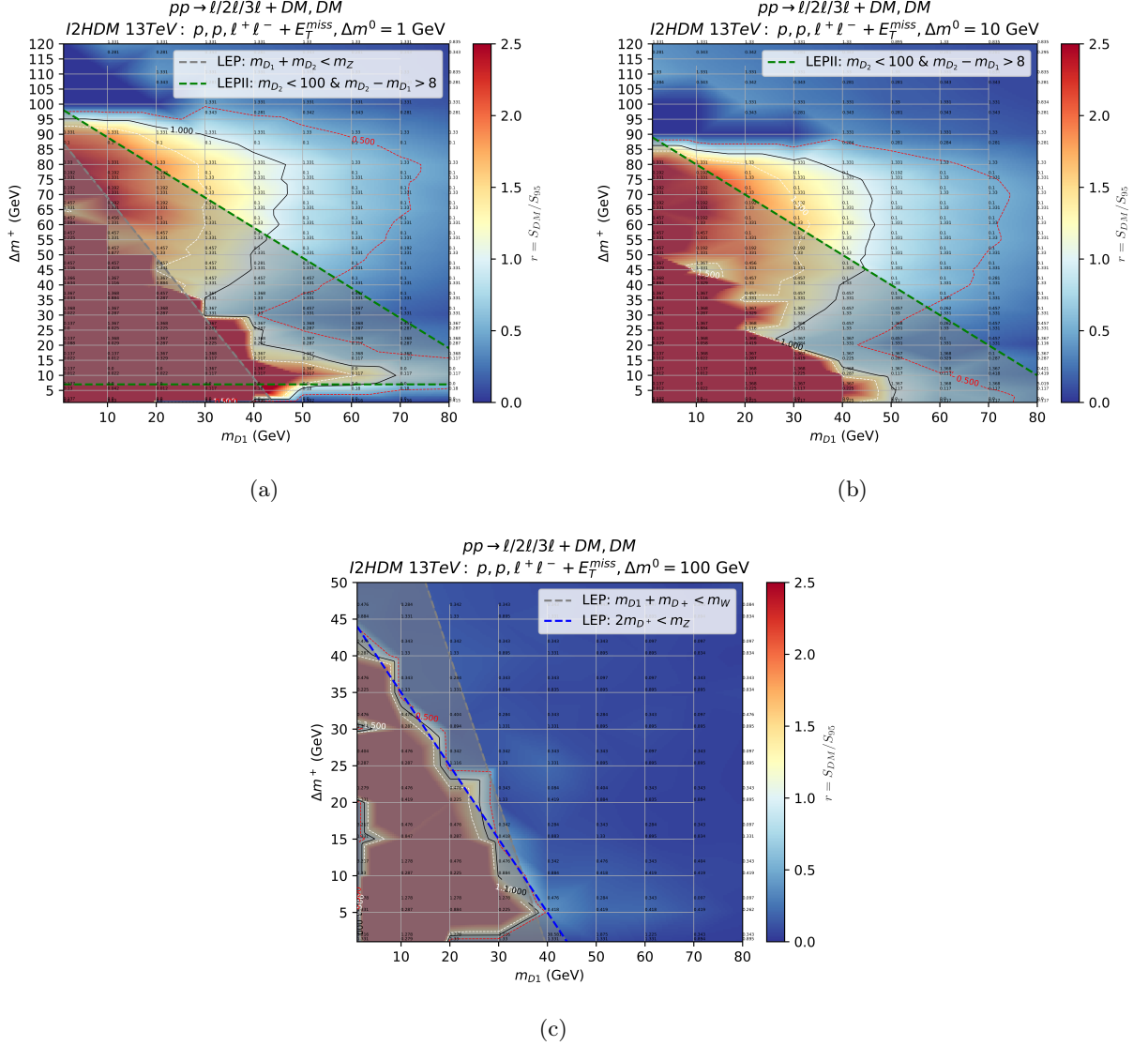


FIG. 19: i2HDM 13 TeV r -value exclusion plots, overlaid with total cross-section yields from 2-lepton(top number) and 3-lepton (bottom number) contributions to r -value. This is with the parametrisation in terms of Δm^+ Δm^0 . Plot (a) shows the case where $\Delta m^0 = 1$ GeV, while plot (b) shows $\Delta m^0 = 10$ GeV and plot (c) shows $\Delta m^0 = 100$ GeV. These are overlaid with limits from LEP I, LEP II experiments [44, 45].

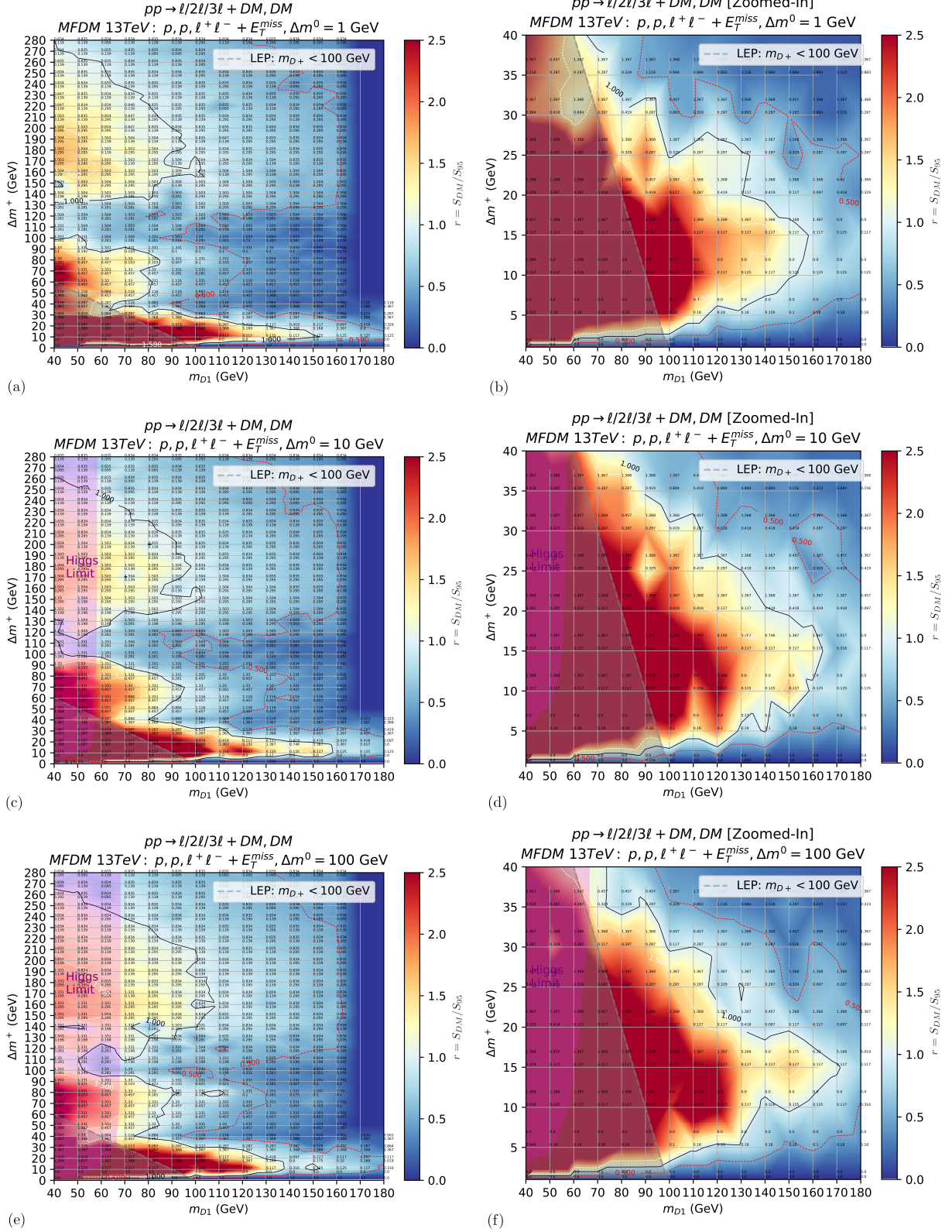


FIG. 20: MFDM 13 TeV r -value exclusion plots overlaid with cross-section yields from 2-lepton(top number) and 3-lepton (bottom number) contributions, for parameter space Δm^+-m_{D1} for $\Delta m^0 = 1$ (a)-(b), 10(c)-(d), 100(e)-(f) GeV. The magenta region and grey region indicate the current Higgs-to-invisible limit[46] of 0.15 branching fraction and LEP bounds on charginos for the fermionic DM case[45] respectively.

Appendix E: Sample Exclusion Formulae

In appendix E we describe the samples and formulae used to understand the tables presented in Appendix F,G. The input samples are separated between A,B and C, in both i2HDM and MFDM cases to improve efficiency.

For i2HDM, set A produces 50,000 events of D^+D^- and D_1D_2 pairs, while specifying the decays $D^\pm \rightarrow \ell^\pm, \nu, D_1$ (via W) and $D_2 \rightarrow \ell^+, \ell^-, D_1$ (via Z). Set B produces 150,000 events of $D^\pm D_2$, while specifying $D_2 \rightarrow \ell^+, \ell^-, D_1$ (via Z) to obtain at least two leptons. Set C produces 100,000 events of the D_1D_1Z production, while specifying leptonic Z decay.

For MFDM, set A produces 50,000 total events, of D^+D^- and D_1D' pairs, while specifying decays of $D^\pm \rightarrow \ell^\pm, \nu, D_1$ (via W) and decays $D' \rightarrow \ell^+, \ell^-, D_1$ (via Z). Set B produces 150,000 $D'D_2$ events, without specifying decays. Set C produces 100,000 events of $D^\pm D'$ and $D^\pm D_2$ pairs, while requiring $D' \rightarrow \ell^+, \ell^-, D_1$ decays, $D_2 \rightarrow \ell^\pm, \nu, D^\pm$ (via W) or $D_2 \rightarrow \ell^-, \ell^+, D'$ decays (via Z). This last set means D' or D^\pm coming from D_2 can also decay hadronically, to fulfil more 2-lepton and 3-lepton thresholds of the analyses.

The exclusion limits between input samples, for the same signal region of a given analysis, can be related by the equation

$$\sigma_A^{95} \epsilon_A = \sigma_B^{95} \epsilon_B = \sigma_C^{95} \epsilon_C \quad (\text{E1})$$

allowing for exclusion r values to be calculated, also noting that

$$r = r_A + r_B + r_C = \frac{\sigma_A^{DM}}{\sigma_A^{95}} + \frac{\sigma_B^{DM}}{\sigma_B^{95}} + \frac{\sigma_C^{DM}}{\sigma_C^{95}}. \quad (\text{E2})$$

Appendix F: i2HDM Cross-Section Limits

In appendix F we present the tables for i2HDM cross-section limits for 2 or 3-lepton final state samples A, B and C. Table V,VI,VII show the results, with $1 < m_{D1} < 80$ GeV, $1 < \Delta m^+ < 120$ GeV, for $\Delta m^0 = 1, 10, 100$ GeV respectively.

m_{D1}	Δm^+	Δm^0	$2\ell \sigma_A^{95}$ (fb)	$\frac{100}{\sqrt{N_{MC}}}$	$2\ell \sigma_B^{95}$ (fb)	$\frac{100}{\sqrt{N_{MC}}}$	$2\ell \sigma_C^{95}$ (fb)	$\frac{100}{\sqrt{N_{MC}}}$	$3\ell \sigma_A^{95}$ (fb)	$\frac{100}{\sqrt{N_{MC}}}$	$3\ell \sigma_B^{95}$ (fb)	$\frac{100}{\sqrt{N_{MC}}}$	$3\ell \sigma_C^{95}$ (fb)	$\frac{100}{\sqrt{N_{MC}}}$
1	5	1	3.26×10^3	71	-	100	6.51×10^4	71	-	-	1.21×10^3	24	-	-
1	10	1	97.0	41	-	100	-	-	-	-	1.21×10^3	24	-	100
1	20	1	1.47×10^3	58	6.63×10^3	71	-	100	-	-	933	21	-	-
1	40	1	1.02×10^5	35	8.17×10^4	58	8.17×10^4	71	-	-	1.2×10^3	8	-	-
1	60	1	8.84×10^3	45	5.3×10^3	20	2.94×10^4	58	-	-	220	6	-	100
1	80	1	783	11	326	4	1.15×10^3	9	-	-	93.0	6	-	-
10	5	1	698	58	3.14×10^3	71	-	100	-	-	-	-	-	-
10	10	1	161	38	674	45	-	-	-	-	-	-	-	-
10	20	1	287	45	-	100	1.43×10^4	71	-	-	1.87×10^3	30	-	100
10	40	1	1.40×10^4	50	1.29×10^4	28	2.23×10^4	45	-	-	531	5	6.82×10^4	71
10	60	1	4.44×10^3	26	507	5	604	7	-	-	165	5	-	-
10	80	1	150	5	248	4	630	7	-	-	80.0	5	-	-
10	120	1	281	6	1.32×10^3	8	411	6	-	-	62.0	4	-	-
20	5	1	97.0	41	877	71	-	-	-	-	-	-	-	-
20	10	1	140	35	562	41	-	-	-	-	-	-	-	-
20	20	1	4.78×10^3	58	1.08×10^4	50	-	-	-	-	9.32×10^3	21	-	-
20	40	1	6.31×10^3	38	6.02×10^3	21	1.76×10^4	45	-	-	366	7	-	-
20	60	1	247	6	377	4	438	6	-	-	148	5	-	-
20	80	1	91.0	4	230	3	534	6	-	-	62.0	5	-	-
20	120	1	247	6	1.50×10^3	9	321	5	-	100	58.0	4	9.40×10^3	58
40	5	1	3.00×10^3	58	2.25×10^3	29	-	-	-	-	-	-	-	-
40	10	1	344	24	390	15	-	-	-	-	-	-	-	-
40	20	1	797	24	1.39×10^3	18	-	100	-	-	2.18×10^3	10	-	-
40	40	1	315	7	710	6	327	5	-	-	387	4	-	-
40	60	1	99.0	4	300	4	302	5	835	41	114	9	2.00×10^3	45
40	80	1	56.0	3	203	3	325	5	313	25	57.0	6	2.00×10^3	45
40	100	1	171	5	1.06×10^3	7	341	5	-	100	76.0	4	1.41×10^4	71
40	120	1	184	5	1.22×10^3	8	229	4	6.91×10^3	70	46.0	3	1.41×10^4	71
60	5	1	900	32	519	14	-	-	-	-	-	-	-	-
60	10	1	292	22	219	11	-	-	-	-	-	-	-	-
60	20	1	344	24	798	21	-	-	-	-	1.90×10^3	10	-	-
60	40	1	228	6	585	5	236	4	-	100	240	6	-	-
60	60	1	79.0	3	255	4	224	4	836	41	71.0	7	900	30
60	80	1	45.0	3	182	3	248	4	627	35	44.0	5	2.48×10^3	50
60	100	1	139	5	1.03×10^3	7	252	4	952	24	188	6	561	13
60	120	1	168	5	1.43×10^3	8	202	4	-	100	45.0	3	1.41×10^4	71
80	5	1	563	25	267	10	-	-	-	-	-	-	-	-
80	10	1	266	21	151	9	-	-	-	-	-	-	-	-
80	20	1	319	15	414	10	3.95×10^3	38	-	-	1.31×10^3	8	-	-
80	40	1	188	5	536	5	198	4	1.25×10^3	50	255	13	1.10×10^3	33
80	60	1	68.0	3	256	4	198	4	251	22	83.0	7	1.24×10^3	35
80	80	1	39.0	2	176	3	223	4	264	23	44.0	5	830	29
80	100	1	140	5	1.20×10^3	8	232	4	7.03×10^3	71	64.0	4	-	100
80	120	1	271	8	680	7	220	5	439	16	128	5	489	12

TABLE V: i2HDM table of limits on the cross sections for A,B and C samples, for $1 < m_{D1} < 80$ GeV, $1 < \Delta m^+ < 120$ GeV, $\Delta m^0 = 1$ GeV.

m_{D1}	Δm^+	Δm^0	$2\ell \sigma_A^{95}$ (fb)	$\frac{100}{\sqrt{N_{MC}}}$	$2\ell \sigma_B^{95}$ (fb)	$\frac{100}{\sqrt{N_{MC}}}$	$2\ell \sigma_C^{95}$ (fb)	$\frac{100}{\sqrt{N_{MC}}}$	$3\ell \sigma_A^{95}$ (fb)	$\frac{100}{\sqrt{N_{MC}}}$	$3\ell \sigma_B^{95}$ (fb)	$\frac{100}{\sqrt{N_{MC}}}$	$3\ell \sigma_C^{95}$ (fb)	$\frac{100}{\sqrt{N_{MC}}}$
1	5	10	110	43	877	71	-	-	-	-	1.03×10^3	22	-	-
1	10	10	257	66	877	71	-	-	-	-	684	18	-	-
1	20	10	358	50	-	100	1.43×10^4	71	-	-	554	16	-	-
1	40	10	1.10×10^4	50	9.46×10^3	27	-	100	2.28×10^4	58	618	5	-	-
1	60	10	4.75×10^3	27	562	5	1.11×10^3	9	-	100	170	5	-	-
1	80	10	168	5	267	4	1.10×10^3	9	-	-	83.0	5	-	-
1	120	10	296	7	1.52×10^3	9	407	6	-	98	70.0	4	-	-
10	5	10	176	40	-	-	-	-	-	-	-	-	-	-
10	10	10	182	56	585	58	-	-	-	-	-	-	-	-
10	20	10	358	50	1.43×10^4	58	1.43×10^4	71	-	-	1.28×10^4	25	-	-
10	40	10	5.48×10^3	58	3.79×10^3	28	-	100	-	-	403	4	-	-
10	60	10	536	9	409	5	710	7	-	-	144	5	-	-
10	80	10	121	4	267	4	714	7	-	-	74.0	5	-	-
10	120	10	264	6	1.57×10^3	9	336	5	856	22	180	6	1.01×10^3	17
20	5	10	3.07×10^3	52	1.69×10^4	71	-	-	-	-	-	-	-	-
20	10	10	1.41×10^3	49	8.77×10^3	71	-	-	-	-	3.42×10^4	41	-	-
20	20	10	4.19×10^3	45	6.97×10^3	33	1.04×10^4	50	-	-	1.48×10^3	8	-	-
20	40	10	1.17×10^3	13	842	6	461	6	-	-	297	7	-	-
20	60	10	161	5	296	4	554	6	716	38	106	8	2.50×10^3	50
20	80	10	82.0	4	236	3	542	6	455	30	69.0	7	2.50×10^3	50
20	100	10	263	6	1.42×10^3	8	398	5	1.28×10^3	27	200	6	1.14×10^3	18
20	120	10	222	6	1.43×10^3	8	285	5	951	24	153	5	856	16
40	5	10	1.02×10^3	30	544	13	-	-	-	-	-	-	-	-
40	10	10	929	25	1.05×10^3	16	9.50×10^3	58	-	-	3.31×10^3	13	-	-
40	20	10	950	12	1.75×10^3	9	290	5	-	100	865	6	-	100
40	40	10	212	6	445	5	298	5	-	-	197	5	-	-
40	60	10	78.0	3	226	3	379	5	456	30	70.0	7	4.98×10^3	71
40	80	10	60.0	3	214	3	328	5	313	25	67.0	7	2.00×10^3	45
40	100	10	201	5	1.30×10^3	8	266	4	1.14×10^3	26	205	6	797	15
40	120	10	180	5	1.38×10^3	8	205	4	569	18	147	5	553	13
60	5	10	877	39	297	13	-	-	-	-	-	-	-	-
60	10	10	831	38	337	14	-	-	-	-	2.77×10^3	12	-	-
60	20	10	578	9	1.43×10^3	8	218	4	-	-	741	6	-	-
60	40	10	126	4	367	4	218	4	1.00×10^3	45	190	11	1.43×10^3	38
60	60	10	63.0	3	220	3	239	4	386	28	71.0	7	2.47×10^3	50
60	80	10	50.0	3	208	3	269	5	455	30	58.0	6	901	30
60	100	10	185	5	1.51×10^3	9	224	4	772	21	159	6	659	14
60	120	10	165	5	1.19×10^3	8	170	4	-	100	43.0	3	1.41×10^4	71
80	5	10	650	33	161	10	-	-	-	-	-	-	-	-
80	10	10	509	16	476	9	2.00×10^4	71	-	100	1.25×10^5	41	2.42×10^5	71
80	20	10	786	12	1.07×10^3	8	9.13×10^3	29	-	100	717	6	-	-
80	40	10	116	4	331	4	188	4	418	29	125	9	1.65×10^3	41
80	60	10	56.0	3	202	3	200	4	264	23	57.0	6	1.41×10^3	38
80	80	10	47.0	3	199	3	217	4	313	25	50.0	6	1.24×10^3	35
80	100	10	273	8	1.07×10^3	9	254	6	6.94×10^3	70	55.0	4	9.38×10^3	58
80	120	10	202	7	759	8	220	5	-	99	31.0	3	-	100

TABLE VI: i2HDM table of limits on the cross sections for A,B and C samples, for $1 < m_{D1} < 80$ GeV, $1 < \Delta m^+ < 120$ GeV, $\Delta m^0 = 10$ GeV.

m_{D1}	Δm^+	Δm^0	$2\ell \sigma_A^{95}$ (fb)	$\frac{100}{\sqrt{N_{MC}}}$	$2\ell \sigma_B^{95}$ (fb)	$\frac{100}{\sqrt{N_{MC}}}$	$2\ell \sigma_C^{95}$ (fb)	$\frac{100}{\sqrt{N_{MC}}}$	$3\ell \sigma_A^{95}$ (fb)	$\frac{100}{\sqrt{N_{MC}}}$	$3\ell \sigma_B^{95}$ (fb)	$\frac{100}{\sqrt{N_{MC}}}$	$3\ell \sigma_C^{95}$ (fb)	$\frac{100}{\sqrt{N_{MC}}}$
1	5	100	-	-	2.38×10^3	11	628	7	-	-	694	4	-	-
1	10	100	-	-	2.27×10^3	11	591	7	-	-	451	5	6.39×10^4	71
1	20	100	-	-	1.88×10^3	10	450	6	-	-	504	3	6.43×10^4	45
1	30	100	-	-	1.64×10^3	9	386	5	-	-	153	5	-	100
1	40	100	3.59×10^3	50	6.14×10^3	38	4.78×10^3	41	-	-	149	5	1.59×10^4	58
10	5	100	2.05×10^3	38	7.17×10^3	41	-	100	-	-	385	4	-	100
10	10	100	4.78×10^3	58	7.17×10^3	41	-	100	-	-	367	4	-	-
10	20	100	4.19×10^3	45	1.05×10^4	41	1.39×10^4	58	-	-	178	5	-	-
10	40	100	4.11×10^3	25	1.28×10^3	8	279	5	-	99	302	8	856	16
20	5	100	7.36×10^3	41	1.66×10^4	35	2.21×10^4	50	-	-	402	5	6.39×10^4	71
20	10	100	2.81×10^3	50	-	100	-	-	-	-	307	4	-	100
20	20	100	2.81×10^3	50	-	-	-	-	-	-	140	4	-	100
20	40	100	1.85×10^3	17	1.01×10^3	7	228	4	3.45×10^3	49	196	7	728	16
40	5	100	2.99×10^3	38	8.97×10^3	38	1.40×10^4	58	6.43×10^5	58	3.60×10^4	8	3.94×10^4	10
40	10	100	2.45×10^3	24	1.47×10^4	33	1.47×10^4	41	-	100	131	4	-	-
40	20	100	1.20×10^3	24	1.05×10^4	41	-	100	6.92×10^3	70	233	7	498	13
40	40	100	1.14×10^3	13	811	6	195	4	8.05×10^3	69	197	6	511	12
60	5	100	585	17	5.23×10^3	29	2.09×10^4	71	-	98	1.24×10^3	8	2.11×10^3	13
60	10	100	708	18	6.28×10^3	32	1.40×10^4	58	4.06×10^3	49	269	7	535	13
60	20	100	2.44×10^3	24	645	7	251	5	3.32×10^3	48	207	7	536	14
60	40	100	851	14	737	7	183	5	1.55×10^3	56	120	9	375	20
80	5	100	789	25	7.85×10^3	45	8.73×10^3	58	-	95	370	8	612	13
80	10	100	512	16	6.98×10^3	33	1.05×10^4	50	1.10×10^3	48	236	13	609	25
80	20	100	1.46×10^3	18	576	7	196	5	2.22×10^3	68	138	10	513	23
80	40	100	791	14	569	7	189	5	1.45×10^3	29	157	6	519	12

TABLE VII: i2HDM table of limits on the cross sections for A,B and C samples, for $1 < m_{D1} < 80$ GeV, $1 < \Delta m^+ < 120$ GeV, $\Delta m^0 = 100$ GeV.

Appendix G: MFDM Cross-Section Limits

In appendix G we present the tables for MFDM cross-section limits for 2- and 3-lepton final state samples A, B and C. For $40 < m_{D1} < 80$ GeV, $1 < \Delta m^+ < 280$ GeV, tables VIII,IX,X show the results for $\Delta m^0 < 1$ GeV, tables XI,XII,XIII show the results for $\Delta m^0 < 10$ GeV and tables XIVXV,XVI show the results for $\Delta m^0 < 100$ GeV

m_{D1}	Δm^+	Δm^0	$2\ell \sigma_A^{95}$ (fb)	$\frac{100}{\sqrt{N_{MC}}}$	$2\ell \sigma_B^{95}$ (fb)	$\frac{100}{\sqrt{N_{MC}}}$	$2\ell \sigma_C^{95}$ (fb)	$\frac{100}{\sqrt{N_{MC}}}$	$3\ell \sigma_A^{95}$ (fb)	$\frac{100}{\sqrt{N_{MC}}}$	$3\ell \sigma_B^{95}$ (fb)	$\frac{100}{\sqrt{N_{MC}}}$	$3\ell \sigma_C^{95}$ (fb)	$\frac{100}{\sqrt{N_{MC}}}$
40	10	1	975	41	2.93×10^3	41	2.11×10^3	42	-	-	-	-	-	-
40	20	1	2.05×10^3	35	-	100	3.59×10^3	33	-	-	100	8.74×10^3	44	-
40	40	1	2.33×10^3	20	8.37×10^4	71	4.53×10^3	20	-	-	2.05×10^4	32	547	6
40	60	1	3.91×10^3	24	1.81×10^4	30	728	7	-	-	1.37×10^4	45	190	6
40	80	1	2.66×10^3	20	7.13×10^3	19	460	6	-	-	4.69×10^3	33	139	7
40	100	1	665	10	9.98×10^4	71	3.02×10^3	15	-	-	-	-	177	8
40	120	1	275	6	-	-	3.94×10^3	16	-	-	-	-	93	6
40	140	1	182	5	1.50×10^4	26	2.45×10^3	13	-	100	5.93×10^3	45	45	5
40	160	1	113	4	1.61×10^4	27	1.63×10^3	10	-	-	1.77×10^3	20	27	3
40	180	1	90	3	1.25×10^4	24	1.45×10^3	10	-	-	1.06×10^3	15	18	2
40	200	1	73	3	9.02×10^3	20	1.14×10^3	9	-	-	703	13	14	2
40	220	1	59	4	7.46×10^3	28	1.06×10^3	13	-	100	510	16	12	3
40	240	1	549	11	2.36×10^3	14	90	3	-	100	454	15	10	3
40	260	1	605	12	1.81×10^3	12	65	3	-	100	258	11	9	3
40	280	1	426	10	1.25×10^3	10	52	2	-	-	348	13	8	2
60	10	1	5.26×10^3	58	1.18×10^4	50	1.91×10^3	25	-	-	-	-	-	-
60	20	1	552	20	4.30×10^3	32	1.70×10^3	24	-	-	6.84×10^4	58	1.76×10^4	36
60	40	1	956	26	1.08×10^4	50	741	16	-	-	2.56×10^4	35	498	6
60	60	1	4.75×10^3	27	1.66×10^4	29	638	7	-	-	1.71×10^4	50	158	6
60	80	1	2.66×10^3	20	9.98×10^3	22	408	6	-	100	5.27×10^3	28	117	5
60	100	1	611	9	1.13×10^5	71	1.98×10^4	36	-	-	-	-	154	7
60	120	1	233	6	-	100	2.81×10^3	14	-	-	-	100	87	6
60	140	1	135	4	1.61×10^4	27	3.14×10^3	14	-	-	2.33×10^3	23	32	3
60	160	1	98	4	1.41×10^4	25	1.70×10^3	11	-	-	1.27×10^3	17	20	3
60	180	1	82	3	6.83×10^3	17	1.16×10^3	9	-	100	1.39×10^3	26	19	4
60	200	1	642	12	3.05×10^3	16	143	4	-	100	642	12	13	2
60	220	1	605	12	2.28×10^3	13	98	3	-	-	515	11	11	2
60	240	1	522	11	1.57×10^3	11	68	3	-	-	444	15	9	3
60	260	1	421	10	1.29×10^3	10	57	3	-	-	279	12	8	2
60	280	1	469	11	1.07×10^3	9	45	2	-	100	346	16	8	3
80	10	1	1.46×10^3	50	1.60×10^3	30	387	18	-	-	-	-	-	-
80	20	1	494	19	1.79×10^3	20	1.87×10^3	26	-	-	6.84×10^4	58	9.72×10^3	27
80	40	1	736	13	1.32×10^4	32	1.06×10^3	11	3.42×10^4	71	1.46×10^4	27	462	6
80	60	1	7.39×10^3	33	9.07×10^3	21	670	7	-	-	4.57×10^3	26	155	6
80	80	1	2.02×10^3	17	6.24×10^3	18	310	5	-	-	5.15×10^3	58	73	8
80	100	1	508	9	6.65×10^4	58	1.68×10^3	11	-	-	-	-	118	6
80	120	1	228	6	-	100	3.54×10^3	15	-	-	6.03×10^3	38	85	6
80	140	1	124	4	1.41×10^4	25	2.37×10^3	13	-	-	2.01×10^3	21	26	3
80	160	1	95	4	1.61×10^4	27	1.45×10^3	10	-	-	852	14	19	3
80	180	1	75	3	9.02×10^3	20	1.02×10^3	8	-	-	764	13	14	2
80	200	1	535	11	2.72×10^3	15	123	4	-	-	746	19	12	3
80	220	1	579	12	2.91×10^3	15	86	3	-	-	348	13	10	3
80	240	1	421	10	1.46×10^3	11	61	3	-	100	346	9	9	2
80	260	1	444	10	1.36×10^3	10	49	2	-	-	252	11	9	2
80	280	1	405	10	907	9	43	2	-	-	225	10	7	2

TABLE VIII: MFDM table of limits on the cross sections for A,B and C samples, for $40 < m_{D1} < 80$ GeV, $1 < \Delta m^+ < 280$ GeV, $\Delta m^0 = 100$ GeV.

m_{D1}	Δm^+	Δm^0	$2\ell \sigma_A^{95}$ (fb)	$\frac{100}{\sqrt{N_{MC}}}$	$2\ell \sigma_B^{95}$ (fb)	$\frac{100}{\sqrt{N_{MC}}}$	$2\ell \sigma_C^{95}$ (fb)	$\frac{100}{\sqrt{N_{MC}}}$	$3\ell \sigma_A^{95}$ (fb)	$\frac{100}{\sqrt{N_{MC}}}$	$3\ell \sigma_B^{95}$ (fb)	$\frac{100}{\sqrt{N_{MC}}}$	$3\ell \sigma_C^{95}$ (fb)	$\frac{100}{\sqrt{N_{MC}}}$
100	10	1	731	35	1.46×10^3	29	407	19	-	-	-	-	-	-
100	20	1	974	41	2.51×10^3	38	431	19	-	-	2.93×10^4	38	1.32×10^4	31
100	40	1	713	13	1.10×10^4	29	1.07×10^3	11	-	-	2.56×10^4	35	422	6
100	60	1	3.33×10^3	22	1.11×10^4	24	497	6	-	-	7.61×10^3	33	164	6
100	80	1	2.38×10^3	19	6.24×10^3	18	328	5	-	100	1.16×10^3	28	89	9
100	100	1	459	8	3.99×10^4	45	1.46×10^3	10	-	-	-	100	118	6
100	120	1	174	5	-	-	3.57×10^3	15	-	100	-	100	40	5
100	140	1	111	4	1.33×10^4	24	1.73×10^3	11	-	-	1.43×10^3	18	25	3
100	160	1	85	3	1.61×10^4	27	1.45×10^3	10	-	-	727	13	16	2
100	180	1	542	11	5.22×10^3	20	138	4	-	100	515	11	13	2
100	200	1	673	13	2.61×10^3	14	103	4	-	100	477	10	10	2
100	220	1	485	11	2.02×10^3	13	77	3	-	100	410	10	9	2
100	240	1	474	11	1.38×10^3	10	54	3	-	-	278	12	9	2
100	260	1	401	10	963	9	46	2	-	-	301	8	7	2
100	280	1	435	10	869	8	39	2	-	100	270	8	7	2
120	10	1	1.46×10^3	50	2.92×10^3	41	428	19	-	-	-	-	-	-
120	20	1	338	13	2.03×10^3	18	880	14	-	-	2.58×10^5	58	5.03×10^4	31
120	40	1	846	12	9.30×10^3	24	695	8	-	100	1.37×10^4	45	307	8
120	60	1	765	12	1.86×10^4	33	775	8	-	-	7.61×10^3	33	131	5
120	80	1	1.39×10^3	14	8.31×10^3	20	323	5	-	-	3.26×10^3	22	83	4
120	100	1	356	7	1.13×10^5	71	6.54×10^3	21	-	-	1.37×10^4	35	114	4
120	120	1	174	5	5.64×10^4	50	2.46×10^3	13	-	-	4.24×10^3	38	40	5
120	140	1	110	4	1.41×10^4	25	1.91×10^3	11	-	-	1.17×10^3	16	21	3
120	160	1	80	3	8.35×10^3	19	1.69×10^3	11	-	-	963	15	15	2
120	180	1	480	11	4.04×10^3	18	129	4	-	-	583	11	12	2
120	200	1	542	11	2.24×10^3	13	79	3	-	-	457	10	10	2
120	220	1	435	10	1.49×10^3	11	62	3	-	-	354	13	9	3
120	240	1	528	11	985	9	49	2	-	100	258	11	8	2
120	260	1	379	10	1.03×10^3	9	40	2	3.48×10^3	71	230	10	8	2
120	280	1	444	10	802	8	35	2	-	100	211	10	7	2
140	10	1	1.95×10^3	58	1.35×10^3	28	429	19	-	-	-	-	-	-
140	20	1	287	12	2.03×10^3	18	544	11	-	-	2.93×10^4	38	5.92×10^3	21
140	40	1	570	10	1.05×10^4	25	731	8	3.42×10^4	71	2.28×10^4	33	400	5
140	60	1	641	11	1.2×10^4	27	801	8	-	-	4.57×10^3	26	121	5
140	80	1	1.58×10^3	15	5.50×10^3	17	292	5	-	-	3.61×10^3	23	96	5
140	100	1	367	7	4.51×10^4	45	7.89×10^3	23	-	-	1.41×10^4	58	107	6
140	120	1	159	5	7.52×10^4	58	2.90×10^3	14	-	100	5.93×10^3	45	42	5
140	140	1	104	4	1.50×10^4	26	2.28×10^3	12	-	-	1.27×10^3	17	20	3
140	160	1	73	3	8.35×10^3	19	1.30×10^3	9	-	-	852	14	15	2
140	180	1	413	10	2.72×10^3	15	102	3	-	-	561	11	11	2
140	200	1	549	11	2.05×10^3	13	75	3	-	100	443	10	10	2
140	220	1	444	10	1.24×10^3	10	56	3	-	100	389	9	9	2
140	240	1	426	10	1.17×10^3	10	44	2	-	100	1.42×10^3	32	9	3
140	260	1	357	9	797	8	39	2	-	-	312	8	7	2
140	280	1	383	10	659	7	34	2	-	100	277	8	7	1

TABLE IX: MFDM table of limits on the cross sections for A,B and C samples, for $100 < m_{D1} < 140$ GeV, $1 < \Delta m^+ < 280$ GeV, $\Delta m^0 = 1$ GeV.

m_{D1}	Δm^+	Δm^0	$2\ell \sigma_A^{95}$ (fb)	$\frac{100}{\sqrt{N_{MC}}}$	$2\ell \sigma_B^{95}$ (fb)	$\frac{100}{\sqrt{N_{MC}}}$	$2\ell \sigma_C^{95}$ (fb)	$\frac{100}{\sqrt{N_{MC}}}$	$3\ell \sigma_A^{95}$ (fb)	$\frac{100}{\sqrt{N_{MC}}}$	$3\ell \sigma_B^{95}$ (fb)	$\frac{100}{\sqrt{N_{MC}}}$	$3\ell \sigma_C^{95}$ (fb)	$\frac{100}{\sqrt{N_{MC}}}$
160	10	1	418	26	1.34×10^3	27	416	18	-	-	-	-	-	-
160	20	1	375	28	1.04×10^3	27	445	21	-	-	2.56×10^4	35	8.84×10^3	25
160	40	1	496	11	4.57×10^3	19	614	8	-	-	1.71×10^4	29	415	6
160	60	1	672	11	8.37×10^3	22	606	7	-	100	4.57×10^3	26	107	5
160	80	1	1.67×10^3	20	7.36×10^3	24	304	6	-	100	5.60×10^3	45	106	8
160	100	1	907	15	-	100	925	11	-	100	9.89×10^3	58	72	6
160	120	1	139	4	7.52×10^4	58	3.01×10^3	14	-	100	3.71×10^3	35	39	4
160	140	1	93	4	1.19×10^4	23	1.74×10^3	11	-	-	1.27×10^3	17	19	3
160	160	1	409	10	5.22×10^3	20	154	4	-	100	607	12	13	2
160	180	1	449	10	2.61×10^3	14	96	3	-	100	439	10	11	2
160	200	1	397	10	1.55×10^3	11	68	3	-	-	418	10	9	2
160	220	1	417	10	1.28×10^3	10	51	2	-	100	418	17	10	3
160	240	1	444	10	1.03×10^3	9	42	2	-	-	290	8	7	2
160	260	1	366	9	772	8	37	2	-	100	211	10	7	2
160	280	1	417	10	792	8	31	2	-	100	221	7	6	1
180	10	1	570	30	723	20	537	21	-	-	-	-	-	-
180	20	1	913	24	1.20×10^3	16	687	14	-	-	-	-	-	-
180	40	1	537	10	5.58×10^3	18	442	6	-	-	2.05×10^4	32	440	6

TABLE X: MFDM table of limits on the cross sections for A,B and C samples, for $160 < m_{D1} < 180$ GeV, $1 < \Delta m^+ < 280$ GeV, $\Delta m^0 = 1$ GeV.

m_{D1}	Δm^+	Δm^0	$2\ell \sigma_A^{95}$ (fb)	$\frac{100}{\sqrt{N_{MC}}}$	$2\ell \sigma_B^{95}$ (fb)	$\frac{100}{\sqrt{N_{MC}}}$	$2\ell \sigma_C^{95}$ (fb)	$\frac{100}{\sqrt{N_{MC}}}$	$3\ell \sigma_A^{95}$ (fb)	$\frac{100}{\sqrt{N_{MC}}}$	$3\ell \sigma_B^{95}$ (fb)	$\frac{100}{\sqrt{N_{MC}}}$	$3\ell \sigma_C^{95}$ (fb)	$\frac{100}{\sqrt{N_{MC}}}$
40	10	10	975	41	8.77×10^3	71	2.39×10^3	45	-	-	-	-	-	-
40	20	10	1.43×10^3	32	1.43×10^4	58	1.30×10^3	21	-	-	5.13×10^4	50	9.65×10^3	27
40	40	10	1.92×10^3	21	1.66×10^4	35	3.70×10^3	20	-	-	4.77×10^3	15	1.15×10^3	9
40	60	10	821	11	5.12×10^3	16	1.86×10^3	12	-	-	2.08×10^3	17	461	10
40	80	10	438	8	2.73×10^3	12	1.14×10^3	9	-	-	1.67×10^3	16	287	8
40	100	10	731	10	1.25×10^4	25	5.06×10^3	19	-	-	7.03×10^3	41	304	10
40	120	10	366	7	4.87×10^3	16	1.99×10^3	12	-	-	-	100	90	6
40	140	10	211	6	2.63×10^3	11	1.23×10^3	10	-	-	5.93×10^3	45	44	5
40	160	10	127	4	3.22×10^4	38	2.32×10^3	12	-	-	4.03×10^3	30	24	3
40	180	10	103	4	2.25×10^4	32	1.41×10^3	10	-	-	3.16×10^3	27	18	2
40	200	10	564	12	1.51×10^3	11	217	5	-	-	2.11×10^3	22	15	2
40	220	10	435	10	1.41×10^3	11	133	4	-	-	1.23×10^3	24	13	3
40	240	10	379	10	1.18×10^3	10	86	3	-	-	870	20	11	3
40	260	10	413	10	1.03×10^3	9	66	3	-	100	949	21	9	3
40	280	10	369	9	818	8	50	2	-	-	803	20	9	2
60	10	10	532	30	1.60×10^3	30	415	19	-	-	-	-	-	-
60	20	10	749	26	2.59×10^3	28	777	19	-	-	4.10×10^4	45	8.16×10^3	24
60	40	10	597	20	4.78×10^3	33	1.08×10^3	19	-	-	3.80×10^3	14	1.06×10^3	9
60	60	10	594	9	5.12×10^3	16	1.90×10^3	12	-	-	2.86×10^3	20	375	9
60	80	10	370	7	3.02×10^3	12	1.06×10^3	9	-	100	1.85×10^3	16	295	8
60	100	10	537	9	2.22×10^4	33	2.82×10^3	15	-	-	4.69×10^3	33	288	10
60	120	10	288	6	2.51×10^4	33	7.69×10^3	23	-	-	4.69×10^3	33	80	5
60	140	10	171	5	1.61×10^4	27	2.15×10^3	12	-	-	3.71×10^3	35	39	4
60	160	10	122	4	1.61×10^4	27	1.56×10^3	10	-	100	1.23×10^3	17	22	3
60	180	10	95	4	1.13×10^4	22	1.43×10^3	10	-	100	1.14×10^3	16	15	2
60	200	10	74	3	9.81×10^3	21	1.08×10^3	8	-	-	746	19	13	3
60	220	10	409	10	2.05×10^3	13	104	4	-	100	444	15	12	3
60	240	10	426	10	1.79×10^3	12	70	3	-	-	354	13	10	3
60	260	10	348	9	1.51×10^3	11	59	3	-	-	271	11	8	2
60	280	10	316	9	1.04×10^3	9	48	2	-	100	444	18	8	3
80	10	10	450	28	1.25×10^3	27	311	16	-	-	-	-	-	-
80	20	10	388	14	2.99×10^3	22	758	13	-	-	3.42×10^4	41	1.53×10^4	33
80	40	10	960	15	7.80×10^3	24	1.68×10^3	14	-	-	2.97×10^3	12	909	8
80	60	10	665	10	4.64×10^3	15	1.85×10^3	12	-	-	1.90×10^3	17	361	9
80	80	10	368	7	2.89×10^3	12	898	8	-	100	1.12×10^3	13	259	8
80	100	10	447	8	3.33×10^4	41	2.98×10^3	15	-	-	3.84×10^3	30	271	10
80	120	10	215	5	2.25×10^4	32	4.42×10^3	17	-	-	2.81×10^3	26	85	6
80	140	10	139	4	1.50×10^4	26	2.08×10^3	12	-	-	1.70×10^3	20	27	3
80	160	10	108	4	1.07×10^4	22	1.48×10^3	10	-	-	923	14	18	2
80	180	10	89	3	1.19×10^4	23	1.32×10^3	9	-	-	561	11	13	2
80	200	10	435	10	3.13×10^3	16	116	4	-	100	522	16	13	3
80	220	10	360	9	2.50×10^3	14	87	3	-	-	399	9	10	2
80	240	10	363	9	1.32×10^3	10	60	3	-	-	326	12	9	2
80	260	10	342	9	1.13×10^3	9	46	2	-	100	342	13	8	2
80	280	10	311	9	894	8	43	2	-	-	308	8	7	2

TABLE XI: MFDM table of limits on the cross sections for A,B and C samples, for $40 < m_{D1} < 80$ GeV, $1 < \Delta m^+ < 280$ GeV, $\Delta m^0 = 10$ GeV.

m_{D1}	Δm^+	Δm^0	$2\ell \sigma_A^{95}$ (fb)	$\frac{100}{\sqrt{N_{MC}}}$	$2\ell \sigma_B^{95}$ (fb)	$\frac{100}{\sqrt{N_{MC}}}$	$2\ell \sigma_C^{95}$ (fb)	$\frac{100}{\sqrt{N_{MC}}}$	$3\ell \sigma_A^{95}$ (fb)	$\frac{100}{\sqrt{N_{MC}}}$	$3\ell \sigma_B^{95}$ (fb)	$\frac{100}{\sqrt{N_{MC}}}$	$3\ell \sigma_C^{95}$ (fb)	$\frac{100}{\sqrt{N_{MC}}}$
100	10	10	532	30	1.35×10^3	28	257	15	-	-	-	-	-	-
100	20	10	295	12	1.37×10^3	15	598	12	-	-	4.10×10^4	45	1.31×10^4	31
100	40	10	789	13	3.58×10^3	16	1.46×10^3	13	-	100	3.66×10^3	13	1.10×10^3	9
100	60	10	821	12	5.40×10^3	18	1.93×10^3	13	-	-	1.49×10^3	15	372	9
100	80	10	321	7	2.85×10^3	12	947	8	-	100	1.40×10^3	14	256	7
100	100	10	993	15	1.56×10^4	35	2.69×10^3	18	-	-	3.84×10^3	30	236	9
100	120	10	250	6	1.41×10^4	25	3.1×10^3	14	-	-	3.01×10^3	27	66	5
100	140	10	127	4	1.88×10^4	29	1.99×10^3	12	-	-	2.01×10^3	21	24	3
100	160	10	96	4	1.25×10^4	24	1.5×10^3	10	-	-	886	14	16	2
100	180	10	401	10	4.47×10^3	19	149	4	-	-	607	12	13	2
100	200	10	405	10	2.41×10^3	14	100	3	-	-	435	14	12	3
100	220	10	430	10	1.65×10^3	11	67	3	3.48×10^3	71	674	18	10	3
100	240	10	345	9	1.11×10^3	9	54	3	-	100	324	9	8	2
100	260	10	302	9	1.03×10^3	9	43	2	-	100	278	12	8	2
100	280	10	314	9	802	8	38	2	-	-	275	8	7	2
120	10	10	292	22	1.03×10^3	24	236	14	-	-	-	-	-	-
120	20	10	390	26	1.95×10^3	33	359	18	-	100	-	-	2.16×10^3	34
120	40	10	614	12	3.68×10^3	17	1.26×10^3	12	-	-	3.31×10^3	13	1.14×10^3	9
120	60	10	915	13	3.80×10^3	15	1.61×10^3	12	-	-	1.46×10^3	15	312	8
120	80	10	285	7	3.12×10^3	12	748	7	-	-	1.34×10^3	14	223	7
120	100	10	888	15	1.14×10^4	30	1.67×10^3	14	-	-	2.34×10^3	24	176	8
120	120	10	192	5	2.26×10^4	32	2.33×10^3	12	-	-	2.12×10^3	27	39	4
120	140	10	122	4	1.61×10^4	27	1.51×10^3	10	-	-	1.08×10^3	16	20	3
120	160	10	89	3	9.40×10^3	20	1.49×10^3	10	-	-	662	12	15	2
120	180	10	401	10	2.91×10^3	15	134	4	-	100	674	18	13	3
120	200	10	366	9	2.24×10^3	13	87	3	-	-	467	10	11	2
120	220	10	319	9	1.35×10^3	10	62	3	-	100	380	13	10	3
120	240	10	296	8	963	9	50	2	2.37×10^3	71	430	17	9	3
120	260	10	319	9	829	8	41	2	-	100	312	8	7	2
120	280	10	271	8	808	8	36	2	-	100	252	11	7	2
140	10	10	482	28	1.57×10^3	29	295	15	-	-	-	-	-	-
140	20	10	223	10	1.18×10^3	14	448	10	-	100	3.73×10^4	58	1.26×10^4	41
140	40	10	293	16	4.77×10^3	38	773	19	-	-	3.81×10^3	24	566	11
140	60	10	664	11	4.29×10^3	16	1.13×10^3	10	-	-	1.34×10^3	14	270	8
140	80	10	298	7	2.17×10^3	10	835	8	2.51×10^3	71	884	24	202	14
140	100	10	787	14	9.63×10^3	28	1.44×10^3	13	-	100	2.81×10^3	26	197	8
140	120	10	176	5	2.05×10^4	30	2.97×10^3	14	-	-	2.61×10^3	24	32	3
140	140	10	110	4	1.07×10^4	22	2.24×10^3	12	-	100	1.64×10^3	19	19	3
140	160	10	363	9	5.22×10^3	20	173	5	-	-	726	13	14	2
140	180	10	345	9	2.32×10^3	14	101	3	-	100	486	15	12	3
140	200	10	326	9	1.76×10^3	12	76	3	-	-	403	10	9	2
140	220	10	309	9	1.28×10^3	10	54	3	-	100	282	12	9	3
140	240	10	292	8	1.06×10^3	9	46	2	-	100	364	16	9	3
140	260	10	307	9	818	8	38	2	7.39×10^3	71	270	8	7	2
140	280	10	243	8	763	8	32	2	-	100	203	10	7	2

TABLE XII: MFDM table of limits on the cross sections for A,B and C samples, for $100 < m_{D1} < 140$ GeV, $1 < \Delta m^+ < 280$ GeV, $\Delta m^0 = 10$ GeV.

m_{D1}	Δm^+	Δm^0	$2\ell \sigma_A^{95}$ (fb)	$\frac{100}{\sqrt{N_{MC}}}$	$2\ell \sigma_B^{95}$ (fb)	$\frac{100}{\sqrt{N_{MC}}}$	$2\ell \sigma_C^{95}$ (fb)	$\frac{100}{\sqrt{N_{MC}}}$	$3\ell \sigma_A^{95}$ (fb)	$\frac{100}{\sqrt{N_{MC}}}$	$3\ell \sigma_B^{95}$ (fb)	$\frac{100}{\sqrt{N_{MC}}}$	$3\ell \sigma_C^{95}$ (fb)	$\frac{100}{\sqrt{N_{MC}}}$
160	10	10	418	26	783	20	295	15	-	-	-	-	-	-
160	20	10	241	11	951	12	325	9	-	100	6.84×10^4	58	1.15×10^4	29
160	40	10	469	9	3.28×10^3	14	1.04×10^3	10	-	-	3.66×10^3	13	805	8
160	60	10	641	11	4.40×10^3	16	1.32×10^3	11	-	-	2.01×10^3	17	344	9
160	80	10	596	12	3.48×10^3	17	812	10	-	100	1.10×10^3	27	184	13
160	100	10	787	14	9.63×10^3	28	1.35×10^3	13	7.03×10^3	71	2.22×10^3	23	162	8
160	120	10	160	5	1.88×10^4	29	1.77×10^3	11	-	-	2.11×10^3	22	31	3
160	140	10	360	9	6.26×10^3	22	260	6	-	-	1.06×10^3	15	19	3
160	160	10	363	9	3.79×10^3	17	146	4	-	100	653	18	14	3
160	180	10	360	9	2.85×10^3	15	100	3	-	100	536	16	12	3
160	200	10	348	9	1.51×10^3	11	61	3	-	-	382	9	9	2
160	220	10	294	8	1.10×10^3	9	48	2	-	100	252	11	9	2
160	240	10	280	8	1.02×10^3	9	43	2	-	100	338	9	7	2
160	260	10	248	8	703	7	36	2	3.48×10^3	71	211	10	7	2
160	280	10	251	8	732	8	32	2	-	-	253	8	6	1
180	10	10	241	20	940	22	286	15	-	-	-	-	-	-
180	20	10	325	26	770	23	263	16	-	-	-	-	-	-
180	40	10	309	17	1.97×10^3	24	646	17	-	100	4.19×10^3	14	933	8

TABLE XIII: MFDM table of limits on the cross sections for A,B and C samples, for $160 < m_{D1} < 180$ GeV, $1 < \Delta m^+ < 280$ GeV, $\Delta m^0 = 10$ GeV.

m_{D1}	Δm^+	Δm^0	$2\ell \sigma_A^{95}$ (fb)	$\frac{100}{\sqrt{N_{MC}}}$	$2\ell \sigma_B^{95}$ (fb)	$\frac{100}{\sqrt{N_{MC}}}$	$2\ell \sigma_C^{95}$ (fb)	$\frac{100}{\sqrt{N_{MC}}}$	$3\ell \sigma_A^{95}$ (fb)	$\frac{100}{\sqrt{N_{MC}}}$	$3\ell \sigma_B^{95}$ (fb)	$\frac{100}{\sqrt{N_{MC}}}$	$3\ell \sigma_C^{95}$ (fb)	$\frac{100}{\sqrt{N_{MC}}}$
40	10	100	73	35	1.25×10^3	27	710	25	-	-	-	-	-	-
40	20	100	1.83×10^3	33	9.86×10^3	45	2.96×10^3	30	-	-	9.77×10^3	22	5.13×10^3	19
40	40	100	1.53×10^3	30	1.69×10^4	58	3.60×10^3	33	-	-	2.21×10^3	18	513	11
40	60	100	377	8	2.66×10^3	12	1.16×10^3	9	-	100	1.35×10^3	8	274	4
40	80	100	197	5	2.85×10^3	12	540	6	1.14×10^4	71	816	11	156	6
40	100	100	532	9	5.70×10^3	17	2.47×10^3	14	-	-	767	13	196	8
40	120	100	354	7	3.91×10^3	14	2.14×10^3	13	-	-	715	13	128	7
40	140	100	282	7	2.98×10^3	12	1.82×10^3	12	-	-	594	12	102	6
40	160	100	189	5	2.98×10^3	12	1.38×10^3	10	-	-	212	7	42	4
40	180	100	141	5	1.90×10^3	10	903	8	-	-	198	7	30	3
40	200	100	318	9	1.44×10^3	11	276	6	-	100	187	9	24	4
40	220	100	270	8	875	8	195	5	-	100	192	10	20	4
40	240	100	228	7	970	9	121	4	-	100	173	9	17	3
40	260	100	214	7	691	7	106	4	-	99	161	6	13	2
40	280	100	181	7	658	7	81	3	-	100	177	6	12	2
60	10	100	390	26	675	20	466	20	-	-	-	-	-	-
60	20	100	731	35	1.46×10^3	29	573	22	-	-	8.54×10^3	20	5.02×10^3	19
60	40	100	920	14	8.83×10^3	26	1.56×10^3	13	-	-	3.31×10^3	13	516	6
60	60	100	292	7	3.77×10^3	14	820	8	-	-	1.05×10^3	12	177	6
60	80	100	145	5	2.98×10^3	12	485	6	-	-	845	11	157	6
60	100	100	416	8	3.70×10^3	14	1.77×10^3	12	-	100	1.06×10^3	16	247	9
60	120	100	368	7	3.99×10^3	14	2.35×10^3	13	7.03×10^3	71	603	12	135	7
60	140	100	232	6	2.89×10^3	12	1.55×10^3	11	-	100	326	10	60	6
60	160	100	161	5	2.77×10^3	12	1.24×10^3	10	-	100	193	7	35	3
60	180	100	366	9	1.29×10^3	10	326	6	-	100	170	6	28	3
60	200	100	300	8	1.32×10^3	10	222	5	-	-	166	9	21	4
60	220	100	216	7	1.16×10^3	10	148	4	-	-	151	9	17	4
60	240	100	210	7	875	8	107	4	7.38×10^3	71	174	6	14	2
60	260	100	196	7	652	7	79	3	2.37×10^3	71	197	12	17	4
60	280	100	160	6	645	7	65	3	-	-	144	8	11	3
80	10	100	418	27	924	23	203	13	-	-	-	-	-	-
80	20	100	266	21	2.51×10^3	38	404	19	-	-	1.14×10^4	24	3.61×10^3	16
80	40	100	736	13	5.76×10^3	21	1.26×10^3	12	-	-	2.86×10^3	20	365	9
80	60	100	253	6	5.12×10^3	16	814	8	-	100	1.07×10^3	12	184	6
80	80	100	123	4	4.87×10^3	16	447	6	-	-	1.08×10^3	16	132	7
80	100	100	356	7	4.87×10^3	16	2.32×10^3	13	-	-	959	15	171	8
80	120	100	311	7	4.87×10^3	16	1.8×10^3	12	-	-	353	11	77	6
80	140	100	257	6	2.69×10^3	11	1.83×10^3	11	-	100	435	10	91	6
80	160	100	401	10	1.58×10^3	11	480	8	-	-	154	6	31	3
80	180	100	296	8	1.72×10^3	12	257	6	-	100	168	9	25	4
80	200	100	213	7	986	9	167	4	-	100	135	8	21	4
80	220	100	223	7	978	9	119	4	-	-	131	8	16	3
80	240	100	183	7	715	8	89	3	-	100	102	7	13	3
80	260	100	170	6	662	7	73	3	-	100	107	7	12	3
80	280	100	140	6	572	7	60	3	-	100	111	7	11	3

TABLE XIV: MFDM table of limits on the cross sections for A,B and C samples, for $40 < m_{D1} < 80$ GeV, $1 < \Delta m^+ < 280$ GeV, $\Delta m^0 = 100$ GeV.

m_{D1}	Δm^+	Δm^0	$2\ell \sigma_A^{95}$ (fb)	$\frac{100}{\sqrt{N_{MC}}}$	$2\ell \sigma_B^{95}$ (fb)	$\frac{100}{\sqrt{N_{MC}}}$	$2\ell \sigma_C^{95}$ (fb)	$\frac{100}{\sqrt{N_{MC}}}$	$3\ell \sigma_A^{95}$ (fb)	$\frac{100}{\sqrt{N_{MC}}}$	$3\ell \sigma_B^{95}$ (fb)	$\frac{100}{\sqrt{N_{MC}}}$	$3\ell \sigma_C^{95}$ (fb)	$\frac{100}{\sqrt{N_{MC}}}$
100	10	100	522	29	1.88×10^3	32	270	15	-	-	-	-	-	-
100	20	100	195	18	1.95×10^3	33	247	15	-	-	1.03×10^4	22	4.05×10^3	17
100	40	100	764	12	3.49×10^3	14	1.28×10^3	11	-	100	2.47×10^3	11	460	6
100	60	100	211	6	4.25×10^3	15	632	7	1.14×10^4	71	1.18×10^3	13	162	6
100	80	100	119	4	3.70×10^3	14	418	6	2.58×10^3	71	418	16	103	10
100	100	100	261	6	3.84×10^3	14	2.27×10^3	13	-	-	827	14	182	8
100	120	100	348	7	2.43×10^3	10	1.57×10^3	10	-	-	349	11	74	6
100	140	100	162	5	2.85×10^3	12	1.43×10^3	10	-	-	172	6	41	4
100	160	100	302	9	1.87×10^3	12	413	7	-	100	193	10	32	5
100	180	100	224	7	1.19×10^3	10	193	5	-	100	132	5	21	3
100	200	100	221	7	941	9	136	4	-	-	117	7	17	3
100	220	100	186	7	715	8	104	4	-	100	115	7	15	3
100	240	100	163	6	673	7	85	3	-	-	98	7	12	3
100	260	100	154	6	666	7	65	3	-	100	123	5	11	2
100	280	100	134	6	526	6	53	3	-	100	104	7	10	3
120	10	100	202	19	548	18	132	11	-	-	-	-	-	-
120	20	100	266	21	1.60×10^3	30	214	14	-	-	1.37×10^4	26	2.60×10^3	14
120	40	100	542	10	4.53×10^3	16	1.01×10^3	10	-	-	2.56×10^3	11	433	6
120	60	100	208	6	3.77×10^3	14	628	7	-	-	1.11×10^3	13	173	6
120	80	100	110	4	3.33×10^3	13	431	6	627	35	836	24	112	11
120	100	100	439	10	4.04×10^3	18	1.38×10^3	13	-	-	619	11	135	6
120	120	100	421	10	2.61×10^3	14	914	10	-	-	258	9	66	6
120	140	100	306	9	1.84×10^3	12	546	8	-	-	178	6	35	3
120	160	100	233	7	1.67×10^3	12	331	6	-	-	138	6	26	3
120	180	100	218	7	1.08×10^3	9	198	5	-	100	114	5	19	3
120	200	100	205	7	823	8	125	4	-	-	118	8	16	3
120	220	100	147	6	740	8	87	3	3.48×10^3	71	105	7	14	3
120	240	100	136	6	593	7	69	3	-	-	117	5	12	2
120	260	100	144	6	564	7	58	3	-	-	121	5	11	2
120	280	100	137	6	499	6	50	2	2.36×10^3	71	88	8	8	3
140	10	100	376	15	2.06×10^3	21	259	9	-	-	-	-	-	-
140	20	100	271	24	2.09×10^3	38	241	16	-	-	-	-	-	-
140	40	100	507	10	3.35×10^3	14	731	8	-	-	3.11×10^3	12	484	6
140	60	100	185	5	4.34×10^3	15	739	7	-	100	939	12	148	6
140	80	100	103	4	3.12×10^3	12	465	6	-	100	975	19	167	10
140	100	100	430	10	3.05×10^3	16	1.34×10^3	13	-	-	549	14	114	8
140	120	100	345	9	2.50×10^3	14	677	9	7.38×10^3	71	213	7	53	4
140	140	100	248	8	1.87×10^3	12	382	7	-	100	151	6	32	3
140	160	100	223	7	1.35×10^3	10	293	6	7.38×10^3	71	137	6	26	3
140	180	100	184	7	1.06×10^3	9	162	4	-	-	115	5	18	2
140	200	100	172	6	840	8	115	4	-	100	124	5	14	2
140	220	100	159	6	688	7	80	3	3.48×10^3	71	110	7	13	3
140	240	100	142	6	590	7	62	3	-	-	111	5	11	2
140	260	100	120	5	614	7	54	3	-	-	129	5	10	2
140	280	100	124	5	474	6	47	2	-	100	127	8	10	3

TABLE XV: MFDM table of limits on the cross sections for A,B and C samples, for $100 < m_{D1} < 140$ GeV, $1 < \Delta m^+ < 280$ GeV, $\Delta m^0 = 100$ GeV.

m_{D1}	Δm^+	Δm^0	$2\ell \sigma_A^{95}$ (fb)	$\frac{100}{\sqrt{N_{MC}}}$	$2\ell \sigma_B^{95}$ (fb)	$\frac{100}{\sqrt{N_{MC}}}$	$2\ell \sigma_C^{95}$ (fb)	$\frac{100}{\sqrt{N_{MC}}}$	$3\ell \sigma_A^{95}$ (fb)	$\frac{100}{\sqrt{N_{MC}}}$	$3\ell \sigma_B^{95}$ (fb)	$\frac{100}{\sqrt{N_{MC}}}$	$3\ell \sigma_C^{95}$ (fb)	$\frac{100}{\sqrt{N_{MC}}}$
160	10	100	196	18	1.71×10^3	30	196	13	-	-	-	-	-	-
160	20	100	217	19	1.17×10^3	26	194	13	-	100	2.40×10^4	71	7.19×10^3	47
160	40	100	386	12	5.37×10^3	27	725	12	-	-	3.36×10^3	13	416	6
160	60	100	213	6	4.16×10^3	14	659	7	-	-	1.05×10^3	12	174	6
160	80	100	98	4	3.56×10^3	13	409	6	386	28	716	22	129	11
160	100	100	394	10	3.05×10^3	16	1.04×10^3	11	-	-	396	9	101	6
160	120	100	267	8	2.66×10^3	15	672	9	-	-	190	7	50	4
160	140	100	250	8	1.47×10^3	11	397	7	3.48×10^3	71	177	9	38	5
160	160	100	195	7	1.24×10^3	10	243	5	-	-	132	5	22	3
160	180	100	170	6	1.00×10^3	9	142	4	-	100	117	5	18	2
160	200	100	155	6	745	8	106	4	4.92×10^3	58	121	5	14	2
160	220	100	133	6	649	7	72	3	-	-	122	5	13	2
160	240	100	125	5	569	7	60	3	2.37×10^3	71	135	10	12	4
160	260	100	112	5	533	7	52	2	3.47×10^3	71	113	7	10	3
160	280	100	111	5	483	6	44	2	-	100	81	8	8	3
180	10	100	310	14	1.58×10^3	18	209	8	-	-	-	-	-	-
180	20	100	225	20	1.35×10^3	28	142	11	1.25×10^5	71	2.51×10^5	58	2.26×10^5	67
180	40	100	339	12	3.76×10^3	22	566	11	-	-	2.44×10^3	11	421	6

TABLE XVI: MFDM table of limits on the cross sections for A,B and C samples, for $160 < m_{D1} < 180$ GeV, $1 < \Delta m^+ < 280$ GeV, $\Delta m^0 = 100$ GeV.

Appendix H: Example Analyses and Cutflows

In appendix H we present examples of the 13 TeV analyses used for the presented exclusion limits and their cutflows as implemented in CheckMATE.

Analysis: cms_sus_16_048, Signal Region: SR1_weakino_1low_mll_1

	Cuts
$mT(\ell[0]/\ell[1], E_T^{miss})$	$< 70 \text{ GeV}$
$mT(p_{\ell[0]}, E_T^{miss})$	$< 70 \text{ GeV}$
$mT(p_{\ell[1]}, E_T^{miss})$	$< 70 \text{ GeV}$
E_T^{miss}	$< 200 \text{ GeV}$
$M_{\ell\ell}$	$< 10 \text{ GeV}$

TABLE XVII: Cutflow for cms_sus_16_048, SR1_weakino_1low_mll_1

Analysis: cms_sus_16039, Signal Region: SR_A02

Two out of the three leptons (e or μ) will form an OSSF pair. This is signal region ‘‘A’’ One of the $m_{\ell\ell}$ bins is defined to be below the Z mass ($M_{l\ell} < 75 \text{ GeV}$).

	Cuts
MT	$0 < MT < 100 \text{ GeV}$
p_T^{miss}	$200 < p_T^{miss} < 250 \text{ GeV}$
$M_{\ell\ell}$	$< 75 \text{ GeV}$

TABLE XVIII: Cutflow for cms_sus_16039, SR_A02

Analysis: cms_sus_16_025, Signal Region: SR2_stop_1low_pt_1

The second category corresponds to the two leptons stemming from two different particles, as in the decays of two top squarks, or in two cascades like χ^\pm to W, χ_1 . In these cases, the leptons are not required to have the same flavour.

	Cuts
E_T^{miss}	$< 200 \text{ GeV}$
$p_T(\ell[0])$	$< 12 \text{ GeV}$

TABLE XIX: Cutflow for cms_sus_16_025, SR2_stop_1low_pt_1

Analysis: atlas_conf_2016_096, Signal Region: 2LASF

This analysis searches for D^+, D^- with two lepton final states.

	Cuts
$ m_{ll} - m_Z $	$> 10 \text{ GeV}$
$mT2$	$> 90 \text{ GeV}$

TABLE XX: Cutflow for atlas_conf_2016_096, 2LASF

Analysis: atlas_conf_2016_096, Signal Region: 3LI

This signal region consists of three leptons, targeting the intermediate mass splitting between D2, D1 of order $2 \times m_Z$.

	Cuts
mT	> 110 GeV
$M(SFOS), E$	$[81.2, 101.2]$ GeV
$pT(3rd lep)$	> 30 GeV
E_T^{miss}	> 120 GeV

TABLE XXI: Cutflow for `atlas_conf_2016_096`, 3LI

Analysis: `cms_sus_16_039`, Signal Region: `SR_A03`

This analysis looks for electroweekinos in multilepton final states. This particular signal region requires three e/μ forming at least one opposite-sign same-flavour pair.

	Cuts
MT	$0 < MT < 100$ GeV
p_T^{miss}	$150 < p_T^{miss} < 200$
$M_{\ell\ell}$	< 75 GeV

TABLE XXII: Cutflow for `cms_sus_16_039`, `SR_A03`

-
- [1] P. A. R. Ade et al. Planck 2015 results. XIII. Cosmological parameters. *Astron. Astrophys.*, 594:A13, 2016.
 - [2] George R. Blumenthal, S. M. Faber, Joel R. Primack, and Martin J. Rees. Formation of Galaxies and Large Scale Structure with Cold Dark Matter. *Nature*, 311:517–525, 1984. [[96\(1984\)](#)].
 - [3] James S. Bullock, Tsafir S. Kolatt, Yair Sigad, Rachel S. Somerville, Andrey V. Kravtsov, Anatoly A. Klypin, Joel R. Primack, and Avishai Dekel. Profiles of dark haloes. Evolution, scatter, and environment. *Mon. Not. Roy. Astron. Soc.*, 321:559–575, 2001.
 - [4] Lyndon Evans and Philip Bryant. LHC Machine. *JINST*, 3:S08001, 2008.
 - [5] F. Gianotti et al. Physics potential and experimental challenges of the LHC luminosity upgrade. *Eur. Phys. J. C*, 39:293–333, 2005.
 - [6] Pedro Schwaller and Jose Zurita. Compressed electroweakino spectra at the LHC. *JHEP*, 03:060, 2014.
 - [7] Daniele Barducci, Alexander Belyaev, Aoife K. M. Bharucha, Werner Porod, and Veronica Sanz. Uncovering Natural Supersymmetry via the interplay between the LHC and Direct Dark Matter Detection. *JHEP*, 07:066, 2015.
 - [8] Prospects for searches for staus, charginos and neutralinos at the high luminosity LHC with the ATLAS Detector. Technical report, CERN, Geneva, Dec 2018. All figures including auxiliary figures are available at <https://atlas.web.cern.ch/Atlas/GROUPS/PHYSICS/PUBNOTES/ATL-PHYS-PUB-2018-048>.
 - [9] Searches for light higgsino-like charginos and neutralinos at the HL-LHC with the Phase-2 CMS detector. 11 2018.
 - [10] Alexander Belyaev, Stefan Prestel, Felipe Rojas-Abatte, and Jose Zurita. Probing dark matter with disappearing tracks at the lhc. *Physical Review D*, 103(9), May 2021.
 - [11] Genevieve Belanger, Beranger Dumont, Andreas Goudelis, Bjorn Herrmann, Sabine Kraml, and Dipan Sengupta. Dilepton constraints in the Inert Doublet Model from Run 1 of the LHC. *Phys. Rev.*, D91(11):115011, 2015.
 - [12] Yu. Andreev, N. Krasnikov, and A. Toropin. Using the $e^\pm\mu^\mp + e_t^{miss}$ and $l^+l^- + e_t^{miss}$ signatures in the search for supersymmetry and constraining the mssm model at lhc, 2007.
 - [13] Kingman Cheung, Duane A. Dicus, B. Dutta, and S. Nandi. Multilepton signatures of gauge mediated susy breaking at cern lep ii. *Physical Review D*, 58(1), Jun 1998.

- [14] Chiara Arina and Maria Eugenia Cabrera. Multi-lepton signatures at LHC from sneutrino dark matter. *JHEP*, 04:100, 2014.
- [15] Subhaditya Bhattacharya, Nirakar Sahoo, and Narendra Sahu. Minimal vectorlike leptonic dark matter and signatures at the LHC. *Phys. Rev.*, D93(11):115040, 2016.
- [16] The ATLAS Collaboration. The ATLAS experiment at the CERN large hadron collider.
- [17] Geneviève Bélanger, Béranger Dumont, Andreas Goudelis, Björn Herrmann, Sabine Kraml, and Dipan Sengupta. Dilepton constraints in the inert doublet model from run 1 of the lhc. *Physical Review D*, 91(11), Jun 2015.
- [18] Daniel Dercks, Nishita Desai, Jong Soo Kim, Krzysztof Rolbiecki, Jamie Tattersall, and Torsten Weber. CheckMATE 2: From the model to the limit. *Comput. Phys. Commun.*, 221:383–418, 2017.
- [19] Alexander Belyaev, Arran Freegard, Ilya F. Ginzburg, Daniel Locke, and Alexander Pukhov. Decoding dark matter at future e^+e^- colliders. 2021.
- [20] John F. Gunion and Howard E. Haber. The CP conserving two Higgs doublet model: The Approach to the decoupling limit. *Phys. Rev. D*, 67:075019, 2003.
- [21] David Eriksson, Johan Rathsman, and Oscar Stal. 2HDMC: Two-Higgs-Doublet Model Calculator Physics and Manual. *Comput. Phys. Commun.*, 181:189–205, 2010.
- [22] Nilendra G. Deshpande and Ernest Ma. Pattern of Symmetry Breaking with Two Higgs Doublets. *Phys.Rev.*, D18:2574, 1978.
- [23] Alexander Belyaev, Giacomo Cacciapaglia, Igor P. Ivanov, Felipe Rojas-Abatte, and Marc Thomas. Anatomy of the Inert Two Higgs Doublet Model in the light of the LHC and non-LHC Dark Matter Searches. *Phys. Rev.*, D97(3):035011, 2018.
- [24] A. Goudelis, B. Herrmann, and O. Stal. Dark matter in the Inert Doublet Model after the discovery of a Higgs-like boson at the LHC. *JHEP*, 1309:106, 2013.
- [25] P. G. Mercadante C. S. Moon S. Moretti S. F. Novaes L. Panizzi F. Rojas A. Belyaev, T. R. Fernandez Perez Tomei and M. Thomas. Advancing lhc probes of dark matter from the inert two-higgs-doublet model with the monojet signal. *Physical Review D*, 99(1), Jan 2019.
- [26] Alexander Belyaev, Neil D. Christensen, and Alexander Pukhov. CalcHEP 3.4 for collider physics within and beyond the Standard Model. *Comput. Phys. Commun.*, 184:1729–1769, 2013.
- [27] M. Bondarenko, A. Belyaev, L. Basso, E. Boos, V. Bunichev, et al. High Energy Physics Model Database : Towards decoding of the underlying theory (within Les Houches 2011: Physics at TeV Colliders New Physics Working Group Report). 2012.
- [28] Andy Buckley, James Ferrando, Stephen Lloyd, Karl Nordström, Ben Page, Martin Rüfenacht, Marek Schönherr, and Graeme Watt. LHAPDF6: parton density access in the LHC precision era. *Eur. Phys. J. C*, 75:132, 2015.
- [29] Torbjörn Sjöstrand, Stefan Ask, Jesper R. Christiansen, Richard Corke, Nishita Desai, Philip Ilten, Stephen Mrenna, Stefan Prestel, Christine O. Rasmussen, and Peter Z. Skands. An Introduction to PYTHIA 8.2. *Comput. Phys. Commun.*, 191:159–177, 2015.
- [30] J. de Favereau et al. DELPHES 3, A modular framework for fast simulation of a generic collider experiment. *JHEP*, 1402:057, 2014.
- [31] Eric Conte, Benjamin Fuks, and Guillaume Serret. Madanalysis 5, a user-friendly framework for collider phenomenology. *Computer Physics Communications*, 184(1):222–256, Jan 2013.
- [32] https://github.com/agagsgroove/checkmate2/blob/LLP-master/tools/analysis/src/analyses/ATLAS_8TeV/atlas_1403_5294.cc.
- [33] https://github.com/agagsgroove/checkmate2/blob/LLP-master/tools/analysis/src/analyses/ATLAS_8TeV/atlas_higg_2013_03.cc.
- [34] M. Aaboud, G. Aad, B. Abbott, J. Abdallah, O. Abdinov, B. Abeloos, R. Aben, O. S. AbouZeid, N. L. Abraham, and et al. Measurement of the $t\bar{t}z$ and $t\bar{t}w$ production cross sections in multilepton final states using 3.2 fb^{-1} of pp collisions at $\sqrt{s} = 13 \text{ tev}$ with the atlas detector. *The European Physical Journal C*, 77(1), Jan 2017.
- [35] Search for direct top squark pair production and dark matter production in final states with two leptons in $\sqrt{s} = 13 \text{ TeV}$ pp collisions using 13.3 fb^{-1} of ATLAS data. Technical report, CERN, Geneva, Aug 2016. All figures including auxiliary figures are available at <https://atlas.web.cern.ch/Atlas/GROUPS/PHYSICS/CONFNOTES/ATLAS-CONF-2016-076>.
- [36] Search for supersymmetry with two and three leptons and missing transverse momentum in the final state at $\sqrt{s} = 13 \text{ TeV}$ with the ATLAS detector. Technical re-

- port, CERN, Geneva, Sep 2016. All figures including auxiliary figures are available at <https://atlas.web.cern.ch/Atlas/GROUPS/PHYSICS/CONFNOTES/ATLAS-CONF-2016-096>.
- [37] Morad Aaboud et al. Search for electroweak production of supersymmetric states in scenarios with compressed mass spectra at $\sqrt{s} = 13$ TeV with the ATLAS detector. *Phys. Rev. D*, 97(5):052010, 2018.
 - [38] A. M. Sirunyan, A. Tumasyan, W. Adam, F. Ambrogi, E. Asilar, T. Bergauer, J. Brandstetter, E. Brondolin, M. Dragicevic, and et al. Search for electroweak production of charginos and neutralinos in multilepton final states in proton-proton collisions at $\sqrt{s} = 13$ tev. *Journal of High Energy Physics*, 2018(3), Mar 2018.
 - [39] Search for new physics in the compressed mass spectra scenario using events with two soft opposite-sign leptons and missing transverse momentum at $\sqrt{s} = 13$ TeV. Technical report, CERN, Geneva, 2016.
 - [40] Search for new physics in events with two low momentum opposite-sign leptons and missing transverse energy at $\sqrt{s} = 13$ TeV. Technical report, CERN, Geneva, 2017.
 - [41] M. Della Negra et al. CMS: letter of intent by the CMS Collaboration for a general purpose detector at LHC. Technical Report CERN-LHCC-92-003. LHCC-I-1, CERN, Geneva, 1992. Open presentation to the LHCC 5 November 1992, M. Della Negra/CERN, CMS Spokesman.
 - [42] Matteo Cacciari, Gavin P. Salam, and Gregory Soyez. Fastjet user manual. *The European Physical Journal C*, 72(3), Mar 2012.
 - [43] G. Aad, T. Abajyan, B. Abbott, J. Abdallah, S. Abdel Khalek, A. A. Abdelalim, O. Abdinov, R. Aben, B. Abi, and et al. Improved luminosity determination in pp collisions at $\sqrt{s} = 7$ TeV using the atlas detector at the lhc. *The European Physical Journal C*, 73(8), Aug 2013.
 - [44] Erik Lundström, Michael Gustafsson, and Joakim Edsjö. Inert doublet model and lep ii limits. *Physical Review D*, 79(3), Feb 2009.
 - [45] Aaron Pierce and Jesse Thaler. Natural dark matter from an unnatural higgs boson and new colored particles at the tev scale. *Journal of High Energy Physics*, 2007(08):026–026, Aug 2007.
 - [46] A.M. Sirunyan, A. Tumasyan, W. Adam, F. Ambrogi, E. Asilar, T. Bergauer, J. Brandstetter, M. Dragicevic, J. Erö, A. Escalante Del Valle, and et al. Search for invisible decays of a higgs boson produced through vector boson fusion in proton-proton collisions at s=13tev. *Physics Letters B*, 793:520–551, Jun 2019.
 - [47] E. Aprile et al. Dark Matter Results from 225 Live Days of XENON100 Data. *Phys. Rev. Lett.*, 109:181301, 2012.
 - [48] E. Aprile et al. First Dark Matter Search Results from the XENON1T Experiment. *Phys. Rev. Lett.*, 119(18):181301, 2017.
 - [49] Beranger Dumont. MadAnalysis 5 implementation of ATLAS-SUSY-2013-11: di-leptons plus MET.
 - [50] G. Aad, B. Abbott, J. Abdallah, S. Abdel Khalek, O. Abdinov, R. Aben, B. Abi, M. Abolins, O. S. AbouZeid, and et al. Search for direct production of charginos, neutralinos and sleptons in final states with two leptons and missing transverse momentum in pp collisions at $\sqrt{s} = 8$ tev with the atlas detector. *Journal of High Energy Physics*, 2014(5), May 2014.
 - [51] Beranger Dumont. MadAnalysis 5 implementation of ATLAS-HIGG-2013-03.
 - [52] <https://atlas.web.cern.ch/Atlas/GROUPS/PHYSICS/PAPERS/SUSY-2013-11/>.
 - [53] https://checkmate.hepforge.org/validationNotes/atlas_1403_5294.pdf.
 - [54] https://checkmate.hepforge.org/validationNotes/atlas_higg_2013_03.pdf.